International Journal of Fatigue 151 (2021) 106389

Contents lists available at ScienceDirect

International Journal of Fatigue

journal homepage: www.elsevier.com/locate/ijfatigue

Fatigue crack growth behavior of Ni-Cr-Mo-V steel welded joints considering strength mismatch effect

Wei Song [a,*], Ping Wang [b], Di Wan [c], Guian Qian [d], José Correia [e,f], Filippo Berto [c]

[a] School of Mechanical & Electrical Engineering, Xuzhou University of Technology, Xuzhou 221018, China
[b] School of Ocean Engineering, Harbin Institute of Technology, Weihai 264209, China
[c] Department of Mechanical and Industrial Engineering, Norwegian University of Science and Technology (NTNU), Richard Birkelands vei 2b, 7491 Trondheim, Norway
[d] State Key Laboratory of Nonlinear Mechanics, Institute of Mechanics, Chinese Academy of Sciences, Beijing 100190, China
[e] Institute for Sustainability and Innovation in Structural Engineering, University of Coimbra, 3030-790 Coimbra, Portugal
[f] Institute of R&D in Structures and Construction, University of Porto, 4200-465 Porto, Portugal

ARTICLE INFO

Keywords:
10CrNi3MoV steel
Fatigue crack growth
Welded joints
R-ratio effect
Material heterogeneity
Mismatch

ABSTRACT

High strength steel welded joints are usually fabricated by heterogeneous weld metal for reducing the negative impacts of microstructural characteristics and defects on mechanical properties, such as hydrogen embrittlement cracking, joint toughness decreasing, etc. To reflect material heterogeneity in the mechanical characteristics, two kinds of weld filler material are selected to obtain Evenmatched Welded Material (E-WM) and Undermatched Welded Material (U-WM) marine Ni-Cr-Mo-V steel welded joints. The Fatigue Crack Growth (FCG) behaviors of Base Metal (BM) and related welded joints are investigated considering load ratio (0.1, 0.4, 0.7) and specimen state (as-welded and heat-treated) effects. The experimental FCG trends for BM and weldments have been compared with the trends available in standards. The FCG rate (da/dN) results show the U-WM demonstrates higher FCGR curves than BM and E-WM. Additionally, it demonstrates no significant difference about FCGR for E-WM and U-WM under high R-ratios (0.4 and 0.7). Moreover, both E-WM and U-WM in as-welded state presents higher fatigue crack propagation resistance than in the Post Welded Heat Treatment (PWHT) state. The fracture mechanism of FCG was analyzed according to the fatigue crack trajectory in microstructures and fractography. Transgranular fracture behavior were observed with some secondary particles in E-WM, while the intergranular fracture was exhibited with few tiny secondary microcracks in U-WM.

1. Introduction

For most heavy-loading engineering welded structures and components, such as mine excavators, truck cranes, ships, and marine structures, High Strength Steel (HSS) or Ultra-High Strength Steel (UHSS) has an increasing demand for improving the structural performance and energy efficiency by structure lightweight realization. Conventional steels contain ferrite microstructure, whereas some advanced HSS have microstructure comprised of different phases, such as ferrite, bainite, austenite, and martensite [1–4]. However, welding processing for HSS or UHSS is sensitive to hydrogen embrittlement, even at a relatively low hydrogen concentration [5]. The welded joints made by HSS or UHSS have a considerable risk of delayed fracture. The hydrogen-assisted fracture in HSS depends significantly on the final weldment microstructure [4,6–8]. Thus, the interaction between the hydrogen and phase constituents of HSS under different conditions is critical to reveal the hydrogen embrittlement mechanism [5]. Since austenite microstructure is prone to giving a higher hydrogen solubility and more hydrogen trapping sites than ferrite microstructure, the austenite consumable is an effective solution for hydrogen-assisted cracking of post welding for HSS or UHSS.

Except for clarifying the hydrogen-assisted fracture mechanism in HSS, some specific treatments are needed to avoid the hydrogen embrittlement fracture for HSS welded joints. Two methodologies were generally adopted to enhance the hydrogen embrittlement resistance by reducing or replacing the precipitates of grain boundary ferrite and intragranular ferrite, which tend to prejudice the mechanical properties of base metal [9,10]. One strategy is to improve the welding processing to decrease the welding cooling rate, such as decreasing the heat input energy by increasing the welding passes [11], preheating [12], and Post

* Corresponding author.
E-mail address: swingways@hotmail.com (W. Song).

https://doi.org/10.1016/j.ijfatigue.2021.106389
Received 14 April 2021; Received in revised form 8 June 2021; Accepted 14 June 2021
Available online 22 June 2021

Welding Heat Treatments (PWHT) [13]. Another strategy is to replace the ferrite wires from austenite welding wire with higher hydrogen solubility. The essential mechanism of austenitic filler for the HSS grades is based on the considerable hydrogen trapping sites. However, due to the differences in mechanical properties between dissimilar microstructures, the fabrication by austinite welded joints would seriously influence the component structural capability compared with ferritic welded joints. Thus, it is crucial to investigate the underlying mechanical properties of HSS considering welding material mechanical heterogeneity, especially under cyclic loading. Nevertheless, the fatigue crack propagation behavior of welded joints is also an excellent performance for overall integrity reliability. The research of high strength steel fatigue and its weldment properties becomes one of the significant issues for material mechanical properties assessment.

According to the investigations of FCG of weldments, it tends to exert more excellent fatigue crack propagation resistance for the microstructures composed of acicular ferrite [14]. It can be attributed that this formed constituent with high angle grain contours can deflect and block the crack growth, which needs a higher energy demand and enhances the fatigue threshold consequently [15]. In the literature, there are many studies about FCG behavior of HSS welding joints (Q345qD steel [16], 10Ni5CrMoV steel [17], 25Cr2NiMo1V steel [18], NiCrMoV rotor steel [19], X100 steel [20], DP780 dual-phase steel [21], WNQ570 [22], S690 [23] and S960 [24]) at different conditions (Heat input effect [10], welded-repaired state [25], high-pressure hydrogen gas environment [20] and seawater environment [26]) and different welding processes (Gas Metal Arc Welding (GMAW) [17], Submerged Arc Welding (SAW) [10], Tungsten Inert Gas (TIG) [21], Laser shock processing [27]) On the other hand, Wang et al. investigated the FCG behavior of Ni-Cr-Mo-V high strength steel welded joint considering the effects of residual stresses, stress ratio and specimen thickness [17]. The results revealed that the acicular ferrite packet weldments have higher fatigue crack growth resistance than 10Ni5CrMoV steel with tempered sorbite microstructure. Given the technical limitations of the high strength-toughness welded consumables, a feasible strategy is to sacrifice the strength to intense the toughness and finally form the undermatched welded joints. The undermatch effect of S960QL welded joints on FCG behavior has also been studied considering the specimen orientations [24]. According to the statistics of Paris-Erdogan exponents (m) for overmatched, evenmatched, and undermatched cases, the FCG resistance of overmatched cases is lower than that of evenmatched cases. In comparison, the FCG resistance of the evenmatched condition is lower than that of the undermatched condition.

Paris and Erdogan proposed the linear relationship of Fatigue Crack Growth Rate (FCGR) and the Stress Intensity Factor (SIF) range as a double logarithmic scale. As one of the significantly effective factors for weldments, stress ratio R effect on the fatigue near-threshold and crack stable growth stages has been widely surveyed considering residual stress. The effect of residual stress regarding as external secondary stress can be incorporated into the R ratio to illustrate the fatigue crack growth behavior. However, the Paris equation cannot directly depict the R ratio effect; more corrections of this equation are conducted using two-parameters models [28–30] or crack closure models [17,31–33]. Up to now, these two methods have been extensively applied to correlate crack growth data for different materials, service conditions or loading levels. The emphasis is on which physical mechanism is suitable for the fracture behavior illustrations and test data correlations.

On the other hand, the remained residual stress after manufacturing processes of Compact Tension (C(T)) welded specimens exhibits significant effects on the FCGR. The quantitative analysis of residual stress effect on FCGR has been discussed by a combined neutron diffraction experimental and numerical study for S355 structural steel HAZ [34]. It reveals that the residual stresses play a vital role in the FCG behavior of welded structures, especially near the fatigue crack threshold region. The residual stress effect on FCG behavior is more complicated due to the explicitly stress redistribution in the crack propagation processing. Regarding to the size effect on FCG behavior, it has not yet been clearly illustrated by experimental evidences, although the content of plasticity can be used to explain some FCGR results with size variations limitedly [35]. The size effect on FRCG is supported by the fatigue crack growth investigation of C(T) specimens made by Inconel-718 alloy [36]. Additionally, Forth, Newman and Forman found that the FCG behavior in C(T) is strongly supported dependent on the size configurations of thickness and width [37]. The net-section-based fracture mechanics approach was proposed to characterize the unique specimen-size correlation of FCGR data of single-edge-cracked specimens. It also found that the geometric correction factors of fracture mechanics are not adequate to deal with the apparent specimen-size effects [35].

Despite some investigations on fatigue crack growth behaviors of steel weldments under different conditions, few studies have been done earlier on the fatigue resistance and crack growth rates characterization of strength mismatch welded joints. In our previous study, the low cycle fatigue behaviors of 10CrNi3MoV steel and its undermatched weldments have been investigated [38]. To clarify the residual life of related welded components by fracture mechanics theory, the present work focuses on the FCG behavior of 10CrNi3MoV steel welded joints produced by GMAW considering the material heterogeneity effect. Firstly, the material microstructure, tensile properties, and fatigue crack growth were analyzed in detail. The FCGR and related standard codes of base metal and weldments were discussed to assess fatigue crack propagation resistance under the as-welded and PWHT states. Subsequently, fatigue crack propagation mechanisms were examined based on the optical microscope and scanning electronic microscopy (SEM) observations of crack growth paths and crack surfaces. Finally, the primary conclusions were summarized. This study provides useful experimental data for safe designs and life prediction considering the material heterogeneity effect.

2. Materials and experimental methods

2.1. Materials and welding processing

10CrNi3MoV low alloy high strength steel is typically used in shipbuilding and submarine structures with the excellent comprehensive performance of strength and ductility, which has a yield strength of about 700 MPa. Two different filler materials were chosen to manufacture the butt-welded joints. The chemical compositions of base metal (BM), evenmatched, and undermatched filler materials are given in Table 1. Evenmatched butt welded joint with a V-groove was fabricated by Single Pulsed Gas Metal Arc Welding (SP-GMAW) processing by corresponding wire (wire diameter Φ 1.2 mm) in 12 mm sheet. While Gas Metal Arc Welding (GMAW) processing was performed to obtain undermatched welded joints by filling lower strength weld metal (wire diameter Φ 1.2 mm). Multipass butt-welded joints are prepared with double V-grooved design as displayed in Fig. 1, which is taken into account of back-chipping processing. For both evenmatched and undermatched weldments, eleven depositions were carried out to fill the prepared groove. The GMAW welding heat input and torch moving speed were controlled as 0.7–0.85 KJ/mm and 4.5–5.3 mm/s. During the joining process, the interpass temperature was maintained under 80 °C between the passes to avoid the hot cracking [38]. The related welding parameters of butt joints were given in Table 2.

2.2. Monotonic tensile and microhardness tests

The monotonic tensile tests of base metal and weldments were conducted by using a universal testing machine under the strain rate 2×10^{-3}/s at room temperature. A servo-hydraulic strength machine MTS 809 was used for the tests. To evaluate the deformation of specimens, the strain was measured by a linear variable extension meter connected to an amplifier. The tests were aimed at determining the strength characteristics of BM and filler materials.

Microhardness tests were performed on the polished multi-pass

Table 1
Nominal chemical composition of the BM and undermatched weldments (%) [38].

Steel	C	Si	Mn	Cr	Mo	Ni	Cu	V	S	P
10CrNi3MoV/Evenmatched-Welds	0.09	0.29	0.48	0.94	0.4	2.88	–	0.06	0.005	0.011
Undermatched-Welds	0.027	0.243	1.3	0.051	–	1.09	0.05	–	0.0073	0.011

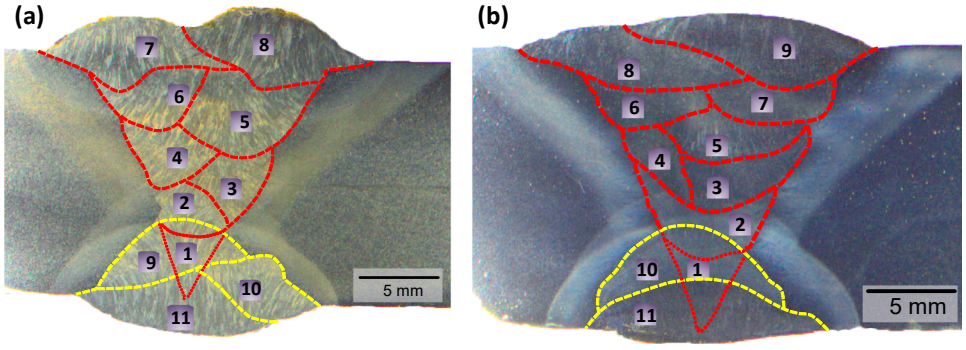

Fig. 1. The multipass butt welded joints schemes considering the back-chipping processing. (a) Evenmatched welds, (b) Undermatched welds.

Table 2
Welding parameters of E-WM and U-WM butt joints [38].

Current (A)	Voltage (V)	Welding speed mm/s	Electrode diameter mm	Shielding gas 80 %Ar-20 %CO_2 L/min	Heat input (KJ/mm)	Interpass temperature °C
140–190	24–28	4.5–5.3	1.2	20	0.7–0.85	<80

welded specimens using a Vickers hardness tester at a load of 500 g and dwell time of 10 s. To avoid any potential effect of strain fields developed by adjacent indentations, adequate distance (400 μm) was spaced between consecutive indentations. These hardness measurements of undermatched and evenmatched welds were conducted along a cross line from welds.

2.3. FCGR experimental methods

Compact Tension (CT) specimens for FCGR tests were cut by Electron Discharge Machining (EDM) from base metal and welded plate along the parallel welding direction to a width of $W = 62.5$ mm following ASTM E647 standard. The weld pads of approximate dimensions 500 × 400 × 16 mm^3 were prepared, and the shape and dimension of specimens are depicted in Fig. 2. Noted that the CT specimens were extracted from the center of welded plate, and the final thickness B of CT specimens was fabricated to 8 mm. Moreover, initial crack length a_0 was taken as 20 mm. The Given fatigue crack initiation direction along with weld bead, the orientation of the notch tips of CT specimens was parallel to weld bead. To obtain stabilized microstructure and reduce the potential residual stress effect on FCGR results, Post-Welding Heat Treatment (PWHT) at 550 °C for 4 h and cooling in the furnace was carried on for BM specimens and most of the welded specimens. Finally, the FCG behaviors of heterogeneity materials considering different states were compared and analyzed.

FCGR tests were conducted at room temperature on an Instron 8802 electro-hydraulic servo testing system. The load capacity of the machine is 25 tons for both tension and compression. The CMOD measuring system based on the compliance method is applied to obtain the FCG rates by accessional fracture extensometer. All the specimens were tested under a constant amplitude sinusoidal loading under three load ratios ($R = 0.1$, 0.4, and 0.7) at a constant frequency of 10 Hz. It should be noted that the frequency has negligible effects on the FCG behavior of steel materials in the air environment [26]. The fatigue propagation crack length was measured continuously by a crack mouth clip gauge based on the compliance method. After the FCGR tests, fatigue crack paths and fracture surfaces were observed by SEM. Before FCG testing, a 3 mm fatigue pre-crack was produced from the notch for CT specimens using the K-decreasing procedure as suggested in [39]. The crack lengths were measured by the compliance method by a highly sensitive Instron 15 mm axial extensometer. The gauge pins were placed in the notches of the CT specimen. The notch geometry details were presented in Fig. 3 (b). It should be noted that a lower bound threshold SIF range between 15 and 20 MPa·$m^{0.5}$ was used to initiate the crack. Additionally, the

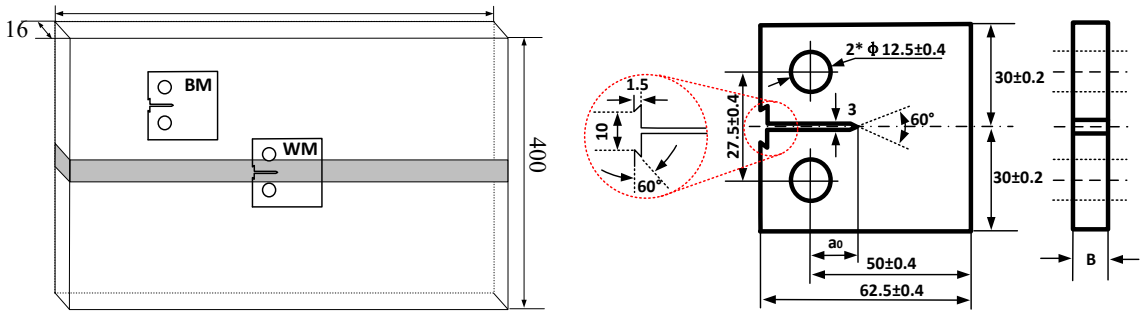

Fig. 2. Fatigue crack growth sample illustration. (a) Schematic diagram of CT specimens from weld plate (mm); (b) Geometry of CT specimens (mm).

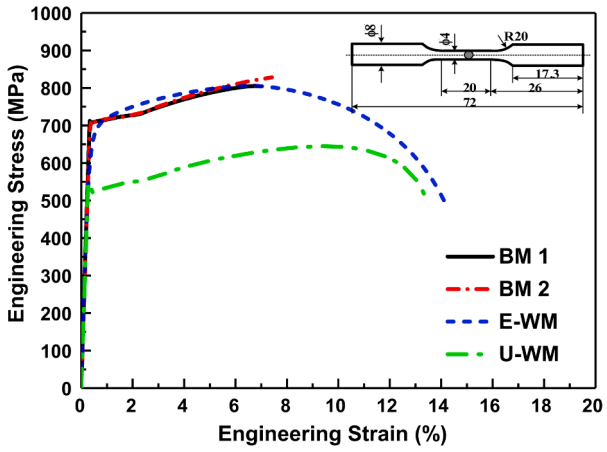

Fig. 3. Monotonic stress-strain curves of 10CrNi3Mov high strength steel and its undermatched welds.

final crack length of stopping test was set as 25 mm.

2.4. Microstructure characterization

Post-mortem fractographic characterization was conducted to understand the microstructural and fracture appearance difference on tested specimens by Optical Microscope (OM) and Scanning Electron Microscope (SEM). The FEG Quanta 650 SEM (Thermo Fisher Scientific Inc., USA) was operated at 20 kV acceleration voltage with an aperture size of 50 μm. Crack profiles were examined by Electron Back Scatter Diffraction (EBSD) system. The samples with fatigue cracks were ground a 2000 grit SiC paper followed by polished using a colloidal silica suspension (OP-S, Struers). Besides, the quantitative information from fracture surfaces was obtained using the built-in software on the cross-section of the specimen. For microstructural analysis, samples were etched with Nital reagent (96 ml ethyl alcohol and 4 ml HNO_3) for 45 s.

2.5. Residual stress measurements

As a destructive technique, the Hole-Drilling (HD) strain gauge method was employed to measure the welding residual stress distributions on the top surface of multipass butt welded joints. A milling processing is conducted to obtain a smooth surface for the measurements of residual stress distribution around the weld joints. Note that a slow milling speed is utilized to avoid additional residual stress during this processing. After the milling process, electro-chemical corrosion is conducted on the newly-formed surface to remove some milling traces. The dimension of three-element strain-gauge rosettes is 11 mm × 11 mm with a 5 mm diameter of gauge circle. The drilled hole diameter is 1.5 mm, and the drilled hole depth is about 2 mm. The calculation of longitudinal and transverse residual stresses was conducted by related equations on the basis of the measured relieved strain.

3. Results

3.1. Results of monotonic tensile tests

Fig. 3 shows the monotonic stress-strain curve of base metal and weldments under the strain rate 2×10^{-3}/s. It can be seen from the figure that the T (the ultimate tensile strength)/Y (0.2% proof yield strength) ratio of 10CrNi3MoV steel reaches 1.07, which indicates that the capability of base metal for hardening is limited. The T/Y ratio of undermatched welds is higher than the base metal, which reaches 1.12. In this Figure, BM, E-WM, and U-WM represent Base Metal, Even-matched Weldments, and Undermatched Weldments, respectively. Table 3 gives the mechanical properties comparisons of these materials under monotonic tension loading. The curves of BM and E-weld reveal a better performance than undermatched weld in terms of yield strength and tensile strength with the values about 710 MPa and 750 MPa. The yield strength and tensile strength of U-weld is lower than other materials, which is about 498 MPa and 559 MPa. Good ductility for U-weld and E-weld can be observed according to the comparison of fracture strain from the tensile curves, while the base metal exhibits bad ductility (fracture strain <10%).

3.2. Microstructure and hardness profiles

The tested microstructures of 10CrNi3MoV high strength steel as Base Metal (BM), Evenmatched weldment (E-WM), and Undermatched weldment (U-WM) by OM and SEM equipment are presented in Fig. 4. These micrographs illustrate the grain boundaries and the non-uniform distribution of precipitates by optical microscope and SEM analyses. The BM showed in Fig. 4(a) (d), which is quenched and tempered, has a fine microstructure mainly composed of Acicular Ferrite (AF), tempered Martensite (M), and Granular Carbides (GC) from metallographic observations. The fast-cooling rate in E-WM further resulted in AF and Bainite (B) grains. Grain boundary Ferrite (GF) also can be seen in the E-WM. Conversely, it was observed that the microstructures in U-WM contain mainly ferrite, partially melted grains with notable pearlite, and precipitation of carbides formed in the grain boundaries. It should be noticed that inclusions in E-WM can contribute positively to nucleation acicular ferrite, which has a positive role in improving the toughness and fatigue strength of the weld [22].

Fig. 5 shows the hardness variations of fusion zone and HAZ for weldments along the transverse section of the E-WM and U-WM welded joints before PWHT. As presented in Fig. 5(a), the soften zone occurs in E-WM welds, which implies that the microhardness of this area is slightly lower than that of base metal. The Coarse Grain HAZ (CGHAZ) covered the area at approximately 2 mm near the fusion zone demonstrated the highest hardness, in which the averaged hardness value of this area is about 350 HV. It implies that the harder martensite phase microstructures than the base metal exist in CGHAZ. It also infers that the Solid-State Phase Transformation (SSPT) occurs during the welding processes. Similar observations are also exhibited in Fig. 5(b). During the welding process, the fusion zone and HAZ experience fast heating and cooling cycle in an extremely short time. The peak temperature of weldments exceeds the melting point, which results in liquidation, solidification, and solid-phase changes. The final hardness of welded joints and corresponding HAZ is determined by its chemical composition and cooling conditions. The HAZ hardness of E-WM welds is comparative with that of U-WM welds. It should be noted that the hardness of E-WM fusion zone is higher than the base metal after welding. According to U-WM plots, it is evident a very pronounced reduction in microhardness at the fusion zone of U-WM due to dissimilar weld filler with base metal, which reaches about 180 HV. The non-uniform distributions of the alloy components, composition, and morphology of welding metal led to a

Table 3
Mechanical properties of test materials.

Steel	Yield strength (MPa)	Tensile strength (MPa)	Young's modulus (GPa)	Poisson's ratio	Elongation at fracture	Kv (J) −20 °C
BM (10CrNi3MoV)	710	750	205	0.3	7.6%	275
E-WM	693	741	205	0.3	14.2%	280
U-WM	498	559	195	0.3	13.4%	260

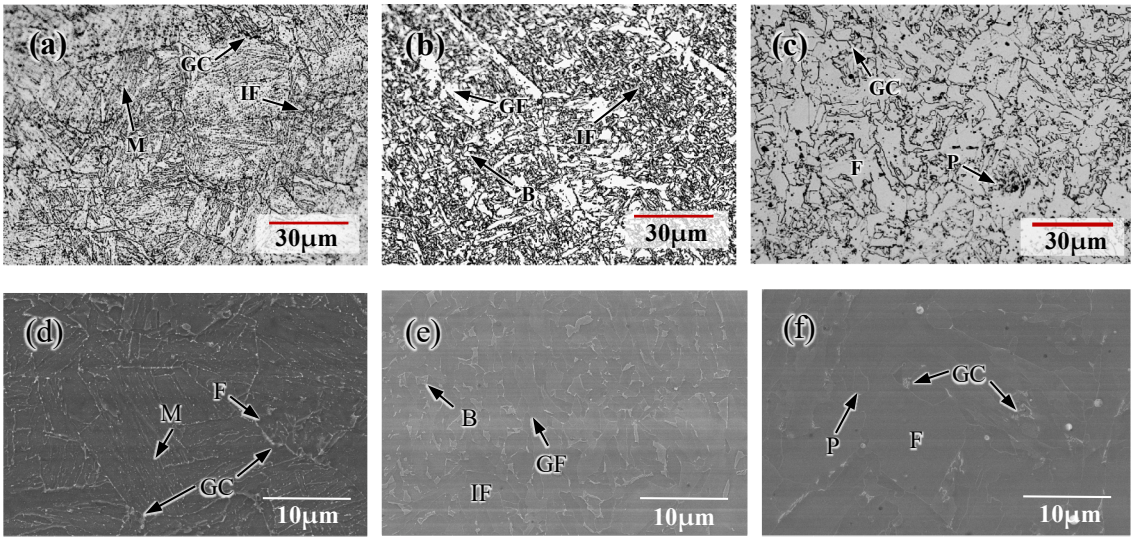

Fig. 4. Optical micrographs (a), (b), (c), and scanning electron microscopy (SEM) figures (d), (e), (f), of BM, E-WM, and U-WM, respectively. Note: AF-Acicular Ferrite, GF-Grain Boundary Ferrite, IF-Intragranular Ferrite, M-Martensite, GC-Granular Carbides, and P-Pearlite from metallographic observations.

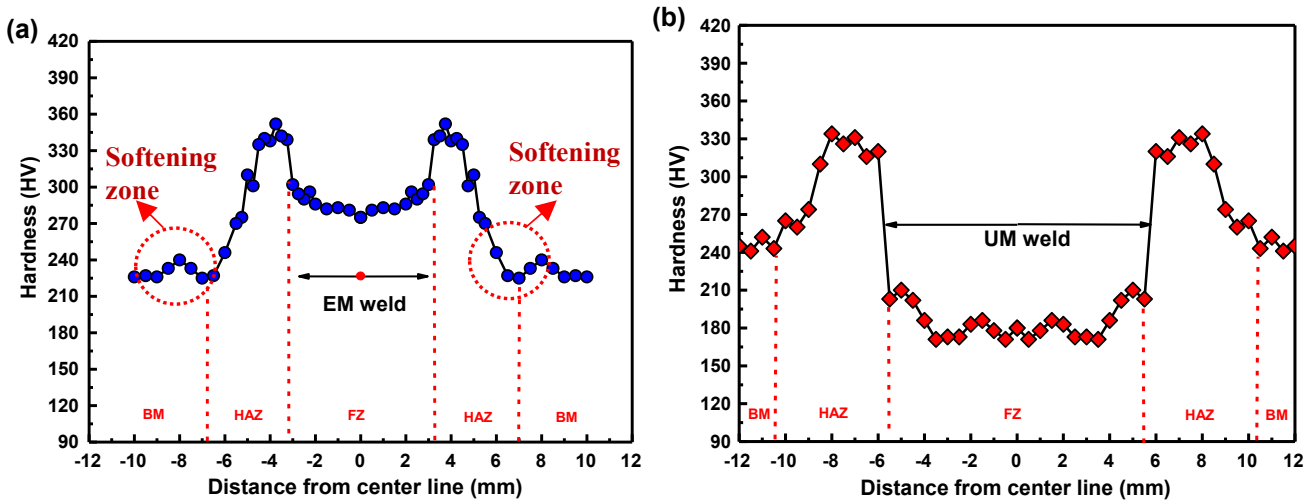

Fig. 5. The hardness distributions of evenmatched welds (a) and undermatched welds (b).

non-uniform distribution of hardness at the welded joint [40]. The non-uniform microstructure distributions also influence fatigue crack growth behaviors of materials.

3.3. Residual stress distribution in welded joints

The welding residual stress induced have a significant influence on the FCGR of welded joints or components. It is necessary to explore the stress contributions of high strength steel welded joint considering the weldment properties, especially for different mismatch welded joints. On the one hand, the mismatch weldment may exert smaller tensile residual stress magnitudes, which make the changing of structural capacity. On the other hand, the stress can be modified from the tensile state to compressive state due to the SSPT effect, which further prolong the fatigue life of weld components. Additionally, the FCGR curves under the as-welded and PWHT state can be illustrated by the stress distributions. Generally, the tensile residual stress will accelerate the FCGR and the compressive residual stress will redundant the fatigue crack propagation. Although parts of residual stresses may be released in small-scale specimen, they play an important role on fatigue behavior and should be considered in design purposes [41]. In order to completely perceive the influence of residual stresses on FCGR behavior, it is essential to consider state of residual stresses during the welding processing, and the redistribution state with the growth of fatigue crack if there is not releasing residual stress.

The longitudinal and transverse residual stresses were simulated according to the E-WM and U-WM material thermal-mechanical properties, which is presented in Fig. 6. In the figure, the LS stands for the residual stress of longitudinal direction, while the TS represents the residual stress of transverse direction. It should be noted that the E-WM and BM will occur the SSPT during the multipass welding. The residual stress in welded joints were calculated with and without the consideration of the SSPT behavior. According the presented results in Fig. 8, the SSPT behavior has a crucial influence on the state and magnitudes of residual stress for both welded joints. In the Fig. 6(a), the high tensile residual stress for the longitudinal direction occurs in the E-WM joint without the SSPT effect. While the transverse residual stress in the weld center tended to be in a compressive state. Since the SSPT behavior modifies the distribution of residual stress in the E-WM joints, the tensile stress zones in longitudinal and transverse directions were transferred from the weld surface to the inside. Significantly, the surface passes in the E-WM joint can induce the apparent compressive residual stress. The

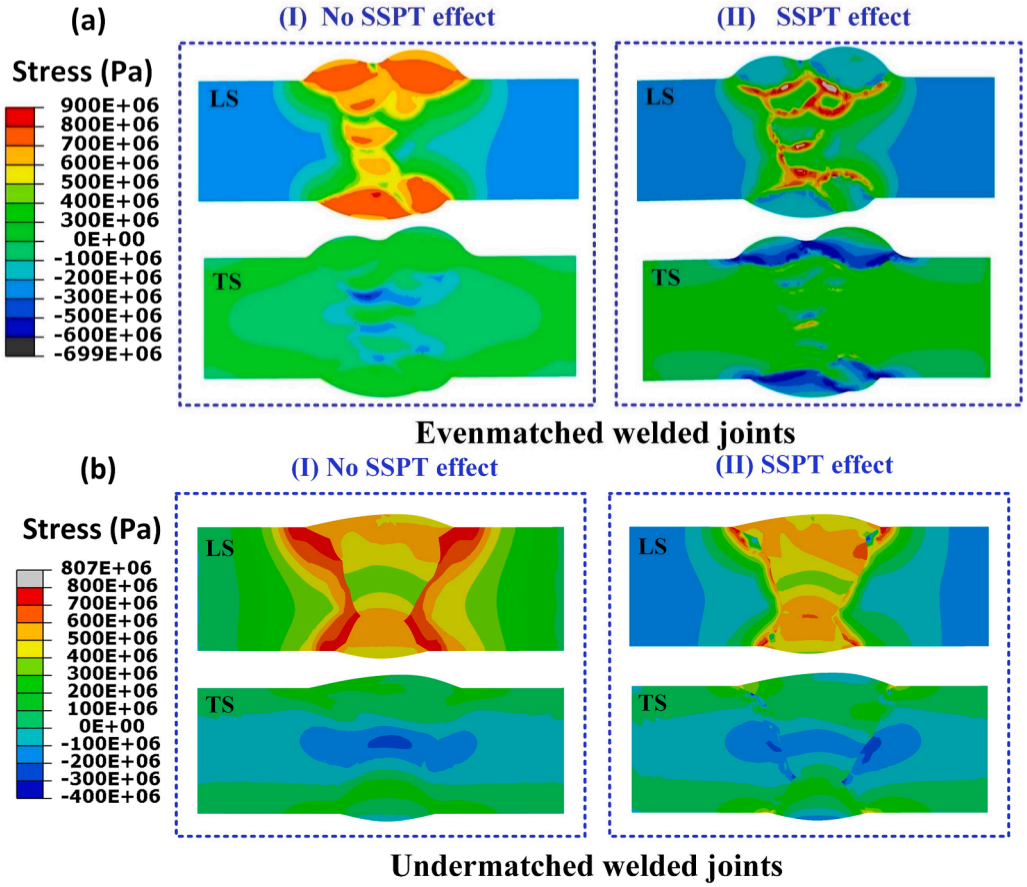

Fig. 6. The residual stress contours considering SSPT effect for evenmatched (E-WM) and undermatched (U-WM) welded joints.

residual stress of U-WM joints is shown in Fig. 6(b), the SSPT behavior of BM in U-WM joints seems has no obvious effect on the residual stress due to the small part subjected to high temperature.

The longitudinal stress is crucial for the FCG behavior on the basis of the extracted direction of C(T) specimens. The comparisons between experimental and calculated residual stress for the E-WM and U-WM are conducted and exhibited in Fig. 7. The calculated residual stresses considering the SSPT behavior in E-WM joint demonstrate more accurate estimations than the results without considering SSPT behavior in Fig. 7(a). The simulated residual stresses in U-WM joint in Fig. 7(b) make good agreements with the experimental data no matter whether the SSPT procedure is involved into the computations.

3.4. Fatigue crack growth behavior

Given the linear log-log relationship da/dN and ΔK, a fatigue crack growth trend can be divided into three regions. (i) Region I represents the threshold stage before the fatigue crack growth, which is

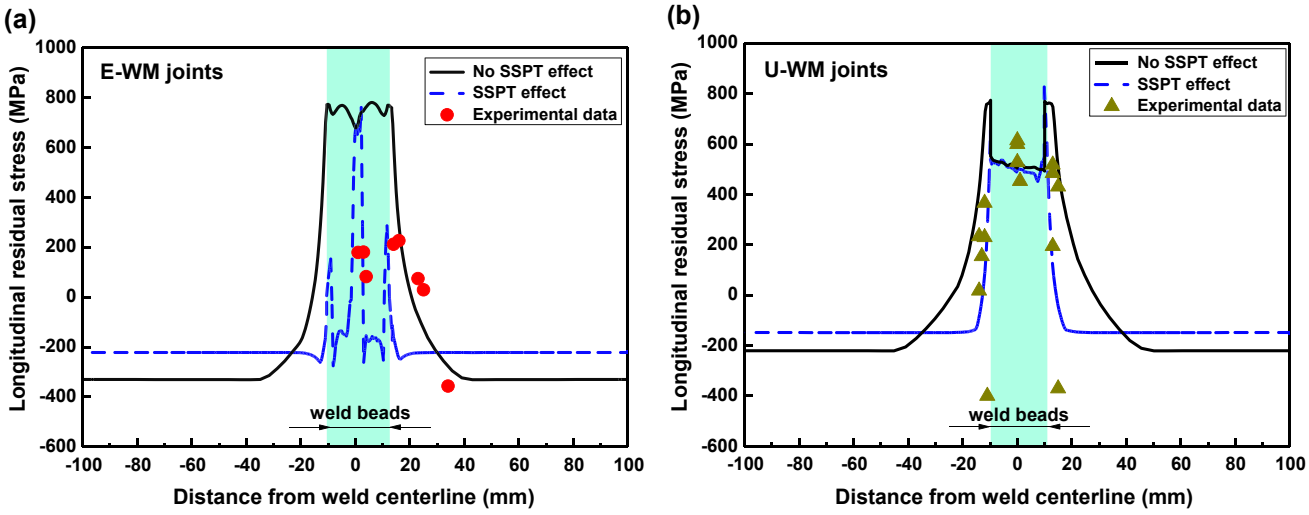

Fig. 7. The residual stress results comparisons between the FE models and experimental data for E-WM and U-WM joints in longitudinal directions. (a) Longitudinal stress in E-WM joint, (b) Longitudinal stress in U-WM joint.

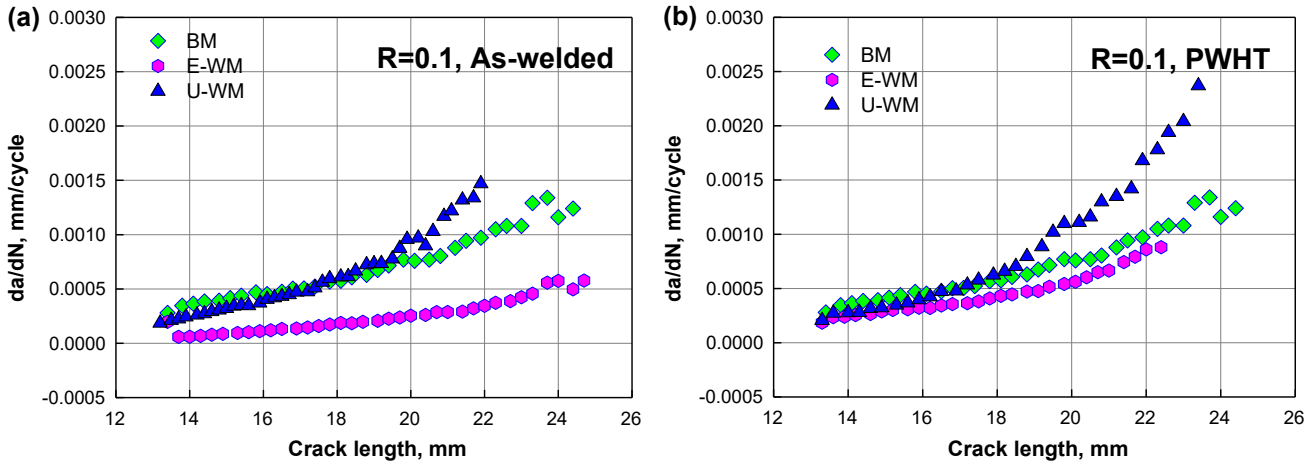

Fig. 8. Fatigue crack growth rate as a function of crack length. (a) the As-welded state, (b) the PWHT state.

characterized as ΔK_{th}. It means that no crack propagation can be detected when the applied ΔK is below the fatigue crack threshold value. (ii) Region II is the fatigue crack growth domain stage. (iii) Region III stands for the final fatigue crack growth accelerating stage. Generally, Region II can be quantitively described by the Paris law:

$$da/dN = C{\cdot}\Delta K^m \tag{1}$$

where a represents the crack length, and N is the number of the cycles, giving da/dN the discrete crack extension/growth per cycle. C and m are material constants in specific testing conditions, while ΔK is the range of the SIF experienced by the material during the fatigue cycles. Generally, the ΔK ranges in the measuring machine are calculated using the formula proposed in ASTM E647 for CT specimens:

$$\Delta K_I = \frac{\Delta P}{B\sqrt{W}}\cdot\frac{(2+\alpha)}{(1-\alpha)^{3/2}}(0.886 + 4.64\alpha - 13.32\alpha^2 + 14.72\alpha^3 - 5.6\alpha^4) \tag{2}$$

where $\alpha = a/W$, a is the crack size, B is the thickness of the specimen, W is the specimen width, and ΔP is the applied load range. Regarding crack growth rate da/dN, it can be computed by the seven-point incremental polynomial technique based on the ASTM E647 standard. Furthermore, regression analysis is conducted under logarithmic coordinates, and FCGR parameters in terms of Paris law can be derived from the relationships between da/dN and ΔK.

According to the BS7910 standard [39], the FCG behavior of a metallic material in Region II, including the base metal and weldments, can be described by two formulations: a simplified Paris law and a two-stage Paris law. The difference between the simplified and two-stage Paris laws lies in the specific characteristic stages. The simplified law mainly clarifies the FCG behavior of Region II, while the two-stage Paris law presents the Region I and Region II stages with different reference line slopes considering the existence of threshold values for base metal and welds. Though the two-stage Paris law gives a more conservative reference line for FCGR than the simplified Paris law, it is convenient to facilitate the comparison procedure with experimental results by the simplified Paris law in our study. The related parameters are collected in Table 4. On the other hand, similar reference lines have also been recommended from IIW standards [42]. According to the recommended parameters from IIW and BS7910, the Paris law parameters for BM and WM are given differently. Furthermore, IIW and BS7910 guidelines of the Paris law curves as reference curves are used to compare with experimental results in the following figures, which are determined with a high survival probability and for a high confidence level. The simplified Paris-law constants for mean curves recommended by BS7910 and IIW for BM and weldments in the air environments were summarized in Table 5. In the table, two types of ΔK units are given for power-law constants, m/cycle and mm/cycle, respectively.

To demonstrate the crack growth behavior of materials without considering the residual stress effect, the FCGR as a function of the crack

Table 5
Simplified fatigue crack growth constants recommended by IIW and BS7910.

Standards	Material	Units	C	m
IIW	BM	N and mm	3×10^{-13}	3
	BM	N and m	9.487×10^{-12}	3
	WM	N and mm	5.21×10^{-13}	3
	WM	N and m	1.65×10^{-11}	3
BS7910 (Simplified)	BM	N and mm	5.21×10^{-13}	3
	BM	N and m	1.65×10^{-11}	3
	WM	N and mm	1.10×10^{-13}	3.1
	WM	N and m	4.91×10^{-12}	3.1

Table 4
Summary of the calculated Paris constants for the different FCGR results of base metal and weldments depicted in Fig. 5. (Units: ΔK in MPa·$m^{1/2}$, da/dN, in m/cycle).

No.	Stress ratio R	P_{max} (KN)	P_{min} (KN)	State	C	m	s^2	Average C	Average m
BM-1	0.1	13.3	1.33	As-welded	1.24×10^{-11}	2.65	0.979	1.24×10^{-11}	2.65
BM-2	0.1	13.3	1.33	PWHT	2.64×10^{-11}	2.46	0.979	4.29×10^{-11}	2.41
BM-3	0.4	16.7	6.7	PWHT	4.28×10^{-11}	2.41	0.948		
BM-4	0.7	16.7	11.7	PWHT	5.96×10^{-11}	2.37	0.937		
E-WM-1	0.1	13.3	1.33	As-welded	2.13×10^{-13}	3.49	0.988	2.13×10^{-13}	3.49
E-WM-2	0.1	13.3	1.33	PWHT	4.08×10^{-12}	2.84	0.943	6.32×10^{-11}	2.45
E-WM-3	0.4	16.7	6.7	PWHT	5.28×10^{-11}	2.37	0.931		
E-WM-4	0.7	16.7	11.7	PWHT	1.33×10^{-10}	2.15	0.967		
U-WM-1	0.1	13.3	1.33	As-welded	4.74×10^{-14}	4.01	0.993	4.74×10^{-14}	4.01
U-WM-2	0.1	13.3	1.33	PWHT	1.56×10^{-14}	4.32	0.993	4.49×10^{-12}	3.47
U-WM-3	0.4	16.7	6.7	PWHT	1.07×10^{-11}	2.78	0.992		
U-WM-4	0.7	16.7	11.7	PWHT	2.78×10^{-12}	3.32	0.987		

length for base metal and weldments under as-welded and PWHT states at $R = 0.1$ was plotted in Fig. 8. An exponential linear tendency of these materials results was observed. Fig. 8(a) shows the curves of FCGR versus crack length under an as-welded state for three different materials. It shows that the initial crack length is about 13 mm after pre-cracking. The FCGR of E-WM is evidently lower than that of BM and U-WM with the fatigue crack increases. However, the FCGR values among these three materials under the PWHT state in Fig. 8(b) are comparative at the beginning of the crack growth. With the propagation of crack length, the FCGR values of BM and E-WM are also lower than that of U-WM, which implies that the BM and E-WM have stronger fatigue crack growth resistance.

The FCGR curves of base metal and weldments (E-WM and U-WM) at stress ratio $R = 0.1$ are plotted in Fig. 9. The FCGR comparisons between as-welded and PWHT states were conducted for these three materials. As presented in Fig. 9(a), the FCGR of BM isn't influenced by the PWHT processing, which means no residual stress effect on FCGR in BM. The FCG data on the BM are compared with the simplified Paris-law reference lines recommended by BS7910 and IIW in Fig. 9.

Although the FCGR data were not fitted by the linear relationship in the log-log axes, the discrepancy between the experimental data and IIW or BS7910 recommended lines can be observed obviously. Due to the high survival probability and for a high confidence level for the recommended curves, the FCGR results of BM are significantly lower than the BM recommendation data of simplified law from IIW and BS7910 considering the high confidence level. It further illustrates that the standard codes can derive a safer fatigue life for welded joints by the fracture mechanics' approach.

In Fig. 9(b), it is notable that the FCGR variation in E-WM specimens is affected by PWHT processing. The FCGR against the range of the SIFs ΔK of as-welded state for E-WM at $R = 0.1$ is higher than that of the PWHT state. However, the FCGR of E-WM for two different states is lower than that of BM. It can be seen that from this figure that the FCGR data points fall in below the simplified curves recommended by both BS7910 and IIW. It suggests that for the range of obtained SIFs, the simplified Paris-law recommended by the standard codes provide a conservative estimation of weldment behavior. According to the experimental and calculated residual stress distribution of E-WM and U-WM, it demonstrates different residual stress states in different direction. The compressive residual stress in E-WM is shown due to the SSPT during the welding processing, which is illustrated in the above section. Thus, the improvement of FCG resistance for E-WM can be attributed to the existence of compressive residual stress. The compressive residual stress can result in crack closure and further incur the increasing fatigue crack resistance, which is favorable for the reduction of the SIF range of FCGR [43,44].

By contrast, it was observed that the difference between as-welded and PWHT state for U-WM seems not significant at $R = 0.1$ in Fig. 9 (c). The FCGR under the as-welded state is slightly lower than the PWHT state. It demonstrates an opposite behavior for weldments, which can be attributed to the tensile residual stress effect on the fatigue crack growth for weldments. In addition, the FCGR curves of U-WM under as welded and PWHT occurred intersections partly comparing with the FCGR curve of BM. A comparison in terms of collected FCGR curves for the BM and

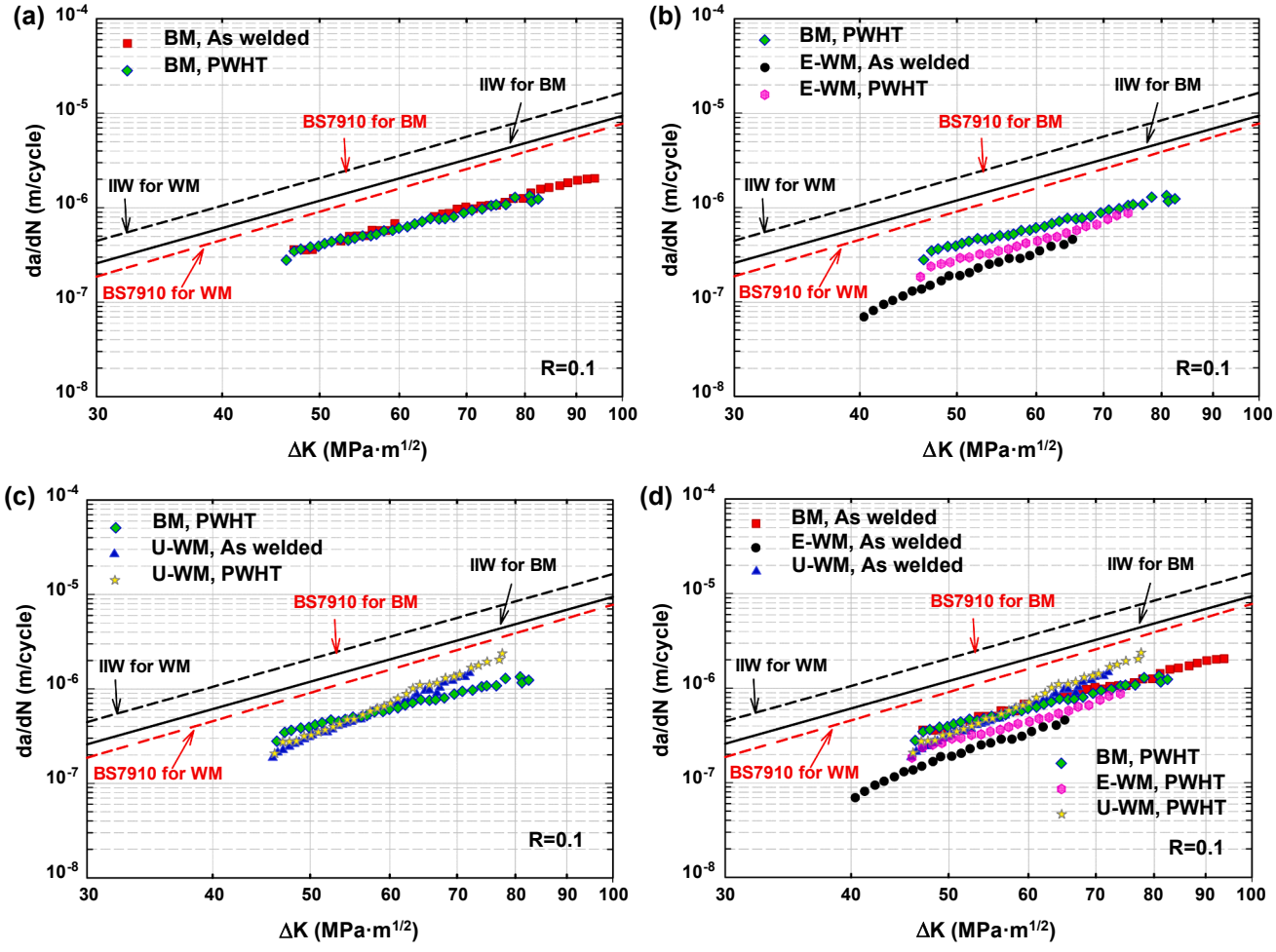

Fig. 9. Effect of specimen state on the FCGR of 10CrNi3MoV steel and its weldments by comparison with standard codes at R = 0.1: (a) BM; (b) E-WM; (c) U-WM; (d) Comparison between BM and WM.

the WM (E-WM and U-WM) was plotted in Fig. 9(d). The overview of FCGR curves for BM and WM are exhibited clearly. The U-WM for PWHT state seems to be the highest FCGR, and E-WM for the as-welded state also shows the lowest FCGR. Finally, the Paris constants C and m from FCGR curves under different states for BM and WM were fitted according to the related equations presented in Table 3.

To quantitatively compare the effects of stress ratio and microstructure on the FCG rate, the experimental investigations for base metal and its weldments under different stress ratios (R = 0.1, 0.4, 0.7) are conducted. Fig. 10 shows the FCGR curves of 10CrNi3MoV steel and its weldment specimens tested with load ratio variations. After eliminating the effect of residual stress in CT specimens, the results of CT specimens are compared under the PWHT state. For base metal in Fig. 10(a), the FCGR curve of E-WM is the lowest one compared with BM and U-WM. The FCGR curve of BM is higher than that of E-WM, while the intersection between the BM and U-WM curves occurs due to different Paris law constant m values. For the low R-ratio (R = 0.1), FCGRs in U-WM have lower resistance than that in the BM and E-WM. For the high R-ratios (0.4 and 0.7), FCGRs of E-WM and U-WM are the same as those of BM in the Paris region, which are presented in Fig. 10(b) and (c). Combined with all tested FCGR curves under different R-ratios into Fig. 10(d), it presents results comparing FCGRs of BM and WM. Although some articles report that the R-ratio is insensitivity in some high strength aerospace materials and bridge structural steels, the R-ratio effects on FCGRs of 10CrNi3MoV steel and its weldments are visible, especially for the E-WM. It also can be observed that FCGRs in the BM and WM become faster as the R ratios increase, which is consistent with the consensus on the R-ratio effect for most metallic materials. On the other hand, regarding the weldment heterogeneity effect on FCGRs under high-stress ratio (R = 0.4 and R = 0.7) for E-WM and U-WM, it does not demonstrate an apparent discrepancy with the results of BM.

3.5. Fatigue crack growth tests data from the literature

The FCGR data on the CT specimens from 10CrNi3Mov steel and its weldments in the study are compared with the available fatigue test data from the literature on different structural steel grades and the BS7910 standards. More information about the test data in this section is collected in Table 6, such as the microstructure, basic mechanical properties, dimensions, welding processing, and fatigue stress ratios. As shown in Table 6, the data collected from the literature are on different grades of the high strength structural steels. Our study only compared the experimental data of base metal and corresponding weldments at stress ratio R = 0.1 to facilitate the assessment procedure. It should be noticed that the simplified recommendation lines from BS7910 for base metal and weldments in the air are employed to compare with the experimental data. The materials used for comparison are SSAB Weldox 960Q steel [24], VOESTALPINE Alform 960M steel [24], S700E steel [24], 10Ni5CrMoV steel [17], S355 steel [23], S690 steel [23], S355G8+M steel [26], DP780 steel [21], Q345qD steel [16], WNQ570 steel [22]. These FCGR data include base metal and its corresponding weldments, which were mainly tested from CT specimens and part of Single Edge Notched Bending (SENB) specimens. Also, the thickness

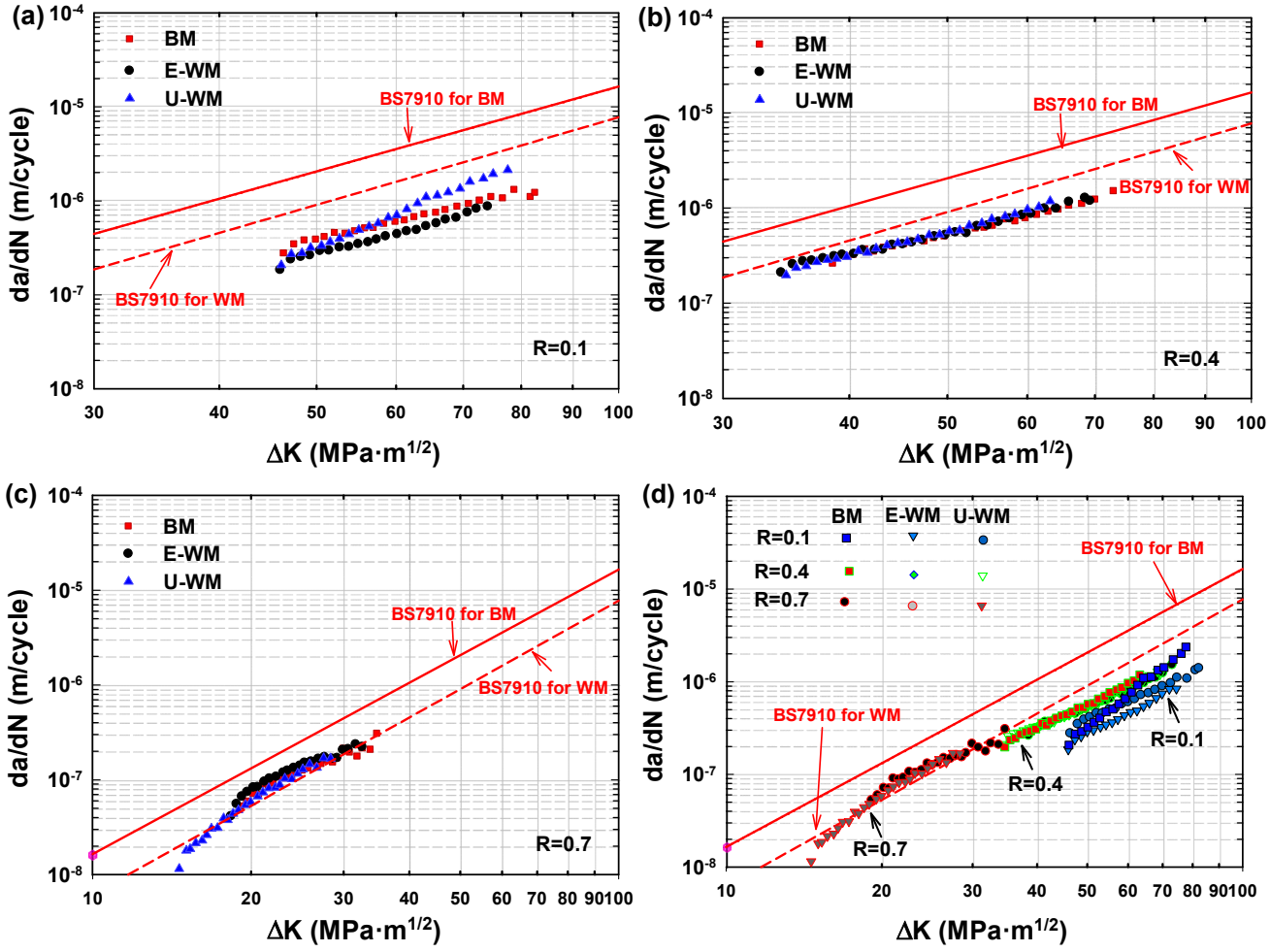

Fig. 10. Effect of stress ratio on the FCGR of 10CrNi3MoV steel and its weldments under PWHT by comparison with standard codes: (a) R = 0.1; (b) R = 0.4; (c) R = 0.7; (d) Summary for different stress ratio.

Table 6
Specimen specifications, microstructure, and the welding process for different steel grades.

Materials	Area	Microstructure	σ_{YS} (MPa)	σ_{UTS} (MPa)	Thickness (mm)	Welding process	PWHT	Stress ratio R
SSAB Weldox 960Q [24]	BM	–	1030	1076	15	–	–	0.1
	FZ1 (Evenmatched)	–	≥930	≥980	15	GMAW	No	0.1
	FZ2 (Undermatched)	–	757	842	15	GMAW	No	0.1
VOESTALPINE Alform 960M [24]	BM	–	1051	1058	15	–	–	0.1
	FZ1 (Evenmatched)	–	≥930	≥980	15	GMAW	No	0.1
	FZ2 (Undermatched)	–	757	842	15	GMAW	No	0.1
S700E [24]	BM	–	791	836	15	–	–	0.1
	FZ1 (Evenmatched)	–	≥790	≥880	15	GMAW	No	0.1
	FZ2 (Overmatched)	–	≥890	≥950	15	GMAW	No	0.1
10Ni5CrMoV [17]	BM	Tempered sorbite	811	864	5, 10	–	–	0.1, 0.25, 0.4, 0.7
	FZ	Martensite, acicular ferrite	613	952	5, 10	TIG	Yes	0.1, 0.25, 0.4, 0.7
S355 [23]	BM	Ferrite, perlite	419	732	8	–	–	0, 0.25
S690 [23]	BM	Needle martensite	766	823	5	–	–	0, 0.25
S355G8+M	BM	Ferrite, perlite	455	544	16	–	–	0.1
	HAZ	–	455	544	16	SAW	No	0.1
DP780 [19]	BM	Martensite, ferrite	546	792	1.5	–		0.1
	FZ	Martensite, ferrite	544	749	1.5	TIG	No	0.1
	HAZ	Tempering martensite, ferrite	–	–	1.5	TIG	No	0.1
Q345qD [16]	BM	Ferrite, pearlite	382	556	13.85	–	–	0.1, 0.2, 0.5
	FZ	Bainite, ferrite, pearlite	580	684	13.5	FCAW	No	0.1, 0.2, 0.5
WNQ570 [22]	BM	Ferrite, bainite	495	568	10	–	–	0.1, 0.2, 0.5
	FZ	Bainite, ferrite and pearlite	569	665	10	MCAW	No	0.1, 0.2, 0.5

range is from 1.5 mm to 50 mm for various materials in this study.

In Fig. 11, the FCGR values from the SENB specimens made by SSAB Weldox 960 steel and VOESTALPINE Alform 960M steel are lower than that of CT specimens made by other steels in the initial crack propagation stage, which is attributed to the difference of geometry constraint between the SENB specimens and CT specimens. FCGR data from some base metals (10CrNi3MoV steel and S690 steel) are near the BS7910 recommendation curve. As seen from this figure, the comparison of FCG trends of different steels exhibits some variations of related fracture parameters of Paris law.

On the other hand, the FCG curves of 10Ni5CrMoV steel, S690 steel, and DP780 dual-phase steel are near and below the BM BS7910 recommendation curve. It can be assumed that the universal parameters from BS7910 BM recommendations are adequate for the FCG reference line. By contrast, most FCGR data from different FZ and HAZ falls below the BS7910 recommendation curve of weldments, which illustrates that the simplified recommendation curves from BS7910 are reliable for assessing FCG behavior. To quantify the characteristic of Paris-Erdogan law parameters, the correlation curve is established to reflect the relationship between C and m in [26].

To quantify the Paris-Erdogen parameters from the FCGR data in the above literature, the correlation between C and m for SSAB Weldox 960Q, VOESTALPINE Alform 960M, and S700E high strength steel and its mismatched weldments in [26] were established. It is shown in Fig. 12 that the logarithmic constant C and exponent m values exhibit a great linear relationship. However, the experimental data from our

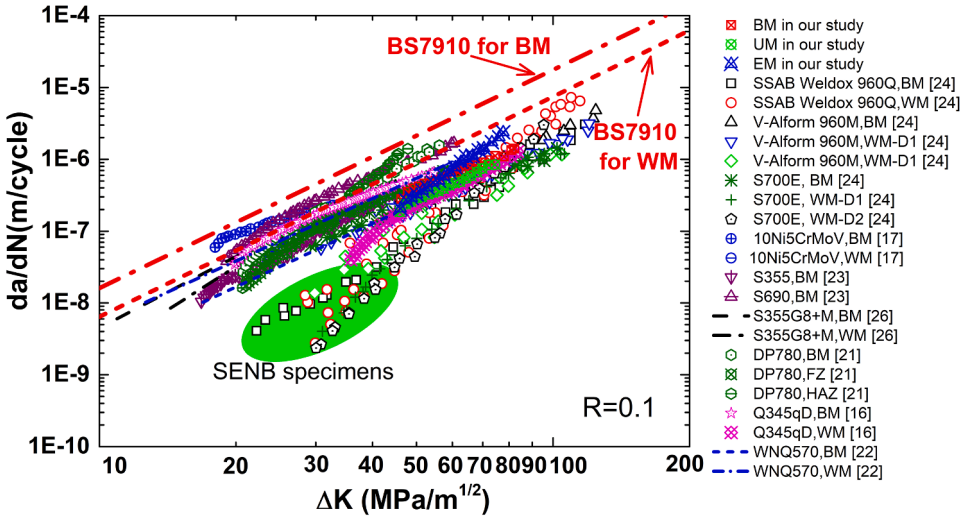

Fig. 11. FCGR on base metal and weldments of structural high strength steel in the air from literature data and BS7910 recommendation curves.

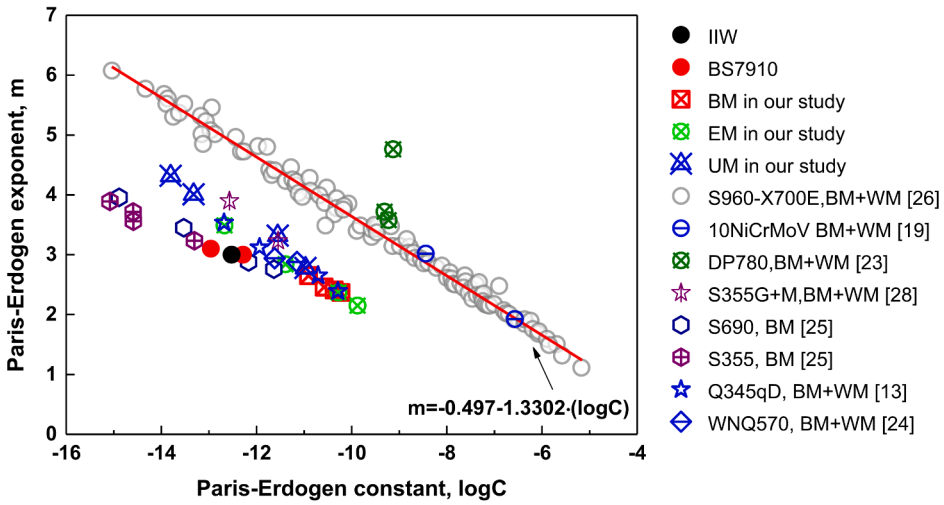

Fig. 12. Correlation of Paris-Erdogen constants C and m from literature about different structural high strength steel.

study and other literature could not drop into the linear curve in [26], and the majority of reference data is below the given reference line, which illustrates that the linear relationship allows reflecting the character of the base metal and welded joints in [26]. Although some fatigue experimental FCGR parameters follow the proposed tendency, the correlation curve is not suitable to illustrate most of the Paris law parameters of other structural high strength steel.

3.6. Fatigue crack path analysis

To understand the microstructural mechanism of fatigue fracture, optical microscopy was carried on a partial area of E-WM and U-WM fracture paths, cut from a typical intermediate crack propagation zone. All fracture samples seem to show a straight crack path by macroscopic observation. Fig. 13 shows different scales of optical micrographs of the crack path for E-WM and U-WM CT specimens at stress ratio $R = 0.1$. As can be seen from the comparison between Fig. 13(a) and (c), the E-WM overall crack growth path is smoother than that of U-WM. The fracture crack of E-WM passes through the mixed bainite and coarse-grained ferrite microstructure region, which results in small crack deflection. By contrast, the crack propagates around the pearlite boundary in U-WM, which leads to large crack deflection in the local area. It indicates that the pearlite has better plastic deformation capability than the mixed microstructure of E-WM. This fracture crack characteristic comparison between E-WM and U-WM is more evident, according to Fig. 13(b) and (d). The pearlite and ferrite microstructures in U-WM demonstrate more tortuous crack propagation paths than that of the larger bainite and coarse-grained ferrite grain in E-WM. Furthermore, a significant difference of FCGR in E-WM and U-WM is reflected in Fig. 10. A similar observation that the crack tends to propagate along the austenite grain contours is presented by Zhu et al. [18].

Fig. 14 shows the EBSD orientation maps of the crack paths from the cross-section in E-WM and U-WM specimens at $R = 0.1$. Fig. 14(a), (b), and (c) represent the fatigue crack initial, stable, and fast propagation stages in CT specimens, respectively. The three crack growth stages can be seen when the fatigue cracks along the grain boundaries and passes through the block of bainite perpendicularly, especially for the stable crack growth stage (Fig. 14(b)). The change of the color a measure for the origination change, which can be supposed as lattice rotation. Thus, it is implied that the local microstructures may have undergone a different deformation mode by the variation of lattice rotation. According to the EBSD observation in Fig. 14(a), the distribution of crystal orientation along the crack growth shows less variation of misorientation close to the crack-tip in the initial stage, which illustrates that the microstructural damage derives from the shear deformation mechanism. On the other hand, the crack branching and secondary cracks near the crack path are observed at $R = 0.1$ in Fig. 10. Along the FCG path presented in Fig. 14(b) and (c), the difference of color shows more substantial heterogeneity than Fig. 14(a), which implies significant plastic deformation during the fatigue crack growth processing. The secondary cracks in the fast propagation stage (Fig. 14(b)) occur more than the initial and stable crack growth stages.

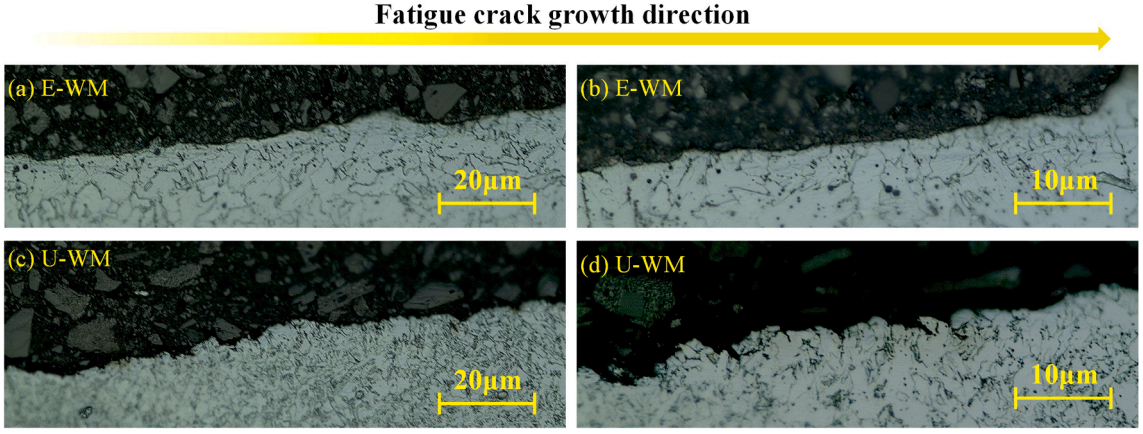

Fig. 13. Fatigue crack propagation path for E-WM and U-WM CT specimens at R = 0.1 under different scales.

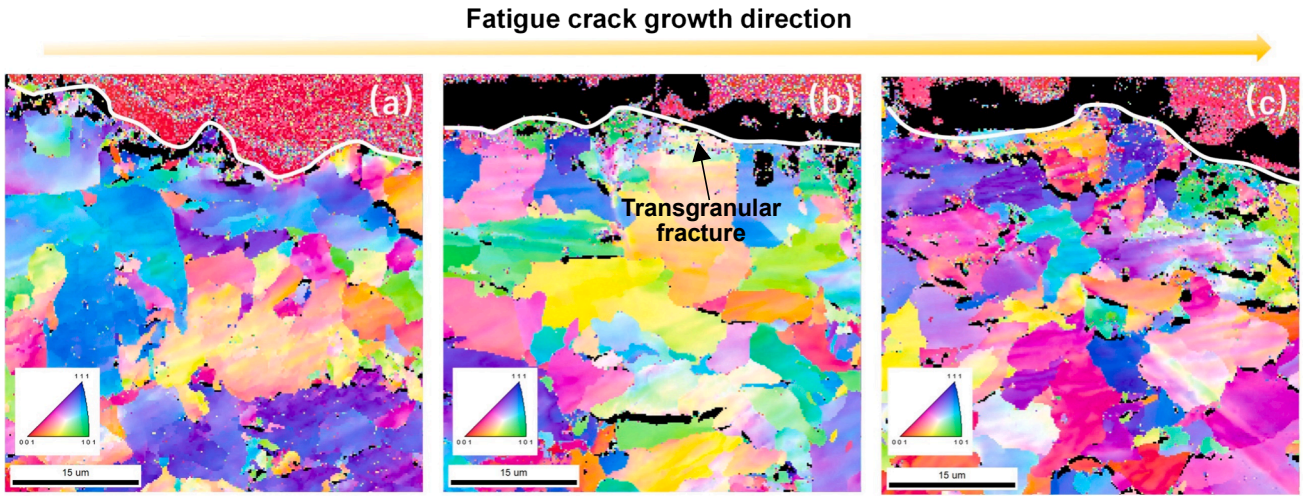

Fig. 14. EBSD observation of fatigue crack growth of the E-WM material. (Global FCG direction is from left to right, and the white lines indicate crack growth paths).

Compared with the E-WM results, the EBSD orientation maps of U-WM are presented in Fig. 15. It can be seen that the grain sizes in U-WM are smaller than the E-WM, and the prominent cracks propagate along the fine grain boundary. Based on the color difference, the crystal orientation in Fig. 15(a) and (c) show substantial heterogeneity, which illustrates significant plastic deformation during crack path deflection.

To directly compare the deformation mechanisms between the evenmatched welds and undermatched welds, the Kernel Average Misorientation (KAM) (0–10°) investigation on fracture paths has been performed on E-WM and U-WM CT specimens, which is presented in Fig. 16 and Fig. 17. Local misorientation is intrinsic lattice defects in GNDs, which is used to judge plastic deformation mechanism or dislocation motion. It represents the arithmetic average misorientation of the given pixel versus the neighboring pixels [45]. The local misorientation angle in the vicinity of the crack path reflects the different degrees of plastic deformation. Fig. 16 shows that the local inhomogeneous misorientation distribution of crack propagation occurs dominantly near fatigue crack in E-WM. However, it is worth mentioning that a larger inhomogeneous misorientation area is observed around the crack path in U-WM (Fig. 17) compared with E-WM (Fig. 16), which indicated that relatively severe plastic deformation in U-WM (Fig. 17). Thus, it is inferred that the U-WM exhibits excellent deformation ability than the E-WM during the fatigue crack propagation. In comparison with three different crack growth stages, furthermore, the plastic deformation in the crack extension accelerated stage is heavier than the initial and stable stages for both E-WM and U-WM. While the plastic deformation degree in the crack growth stable stage is lower than the other two stages.

3.7. Fatigue fractography analysis

All the tested E-WM and U-WM CT specimens at $R = 0.1$ have been carried on fractography analysis by different scales. The fracture morphologies of E-WM and U-WM specimens under these regimes by two different specific magnifications (scale bars 10 μm and 50 μm) are presented in Fig. 18 and Fig. 19, respectively. The crack propagation direction of all the fracture surfaces is marked from top to bottom, shown as the yellow arrow. It can be seen from Fig. 18 and Fig. 19 in the plotting scale of 10 μm that the crack growth surface of U-WM has relative rougher fracture surface morphology than that of E-WM, and fracture paths of U-WM are intergranular and highly tortuous. Furthermore, flat surfaces are also observed in E-WM local areas, which is suggested to be formed by transgranular fracture. Thus, E-WM and U-WM demonstrate different fracture mechanisms.

The presence of striations provides information for the failure analysis in component service, the global and local propagation direction, and crack growth rate [46,47]. The presence of fatigue striations characteristic results from the blunt plastic process at the crack tip [48]. To demonstrate the striations of the fracture surface for different specimens, the local fracture surfaces in different regimes are captured in

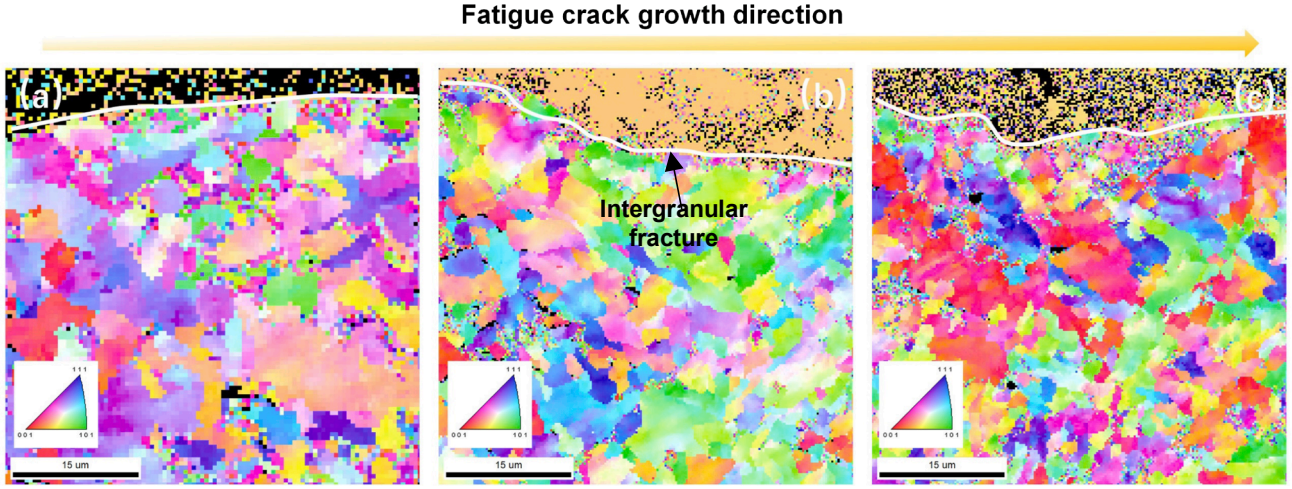

Fig. 15. EBSD observation of fatigue crack growth of the U-WM material. (Global FCG direction is from left to right, and the white lines indicate crack growth paths).

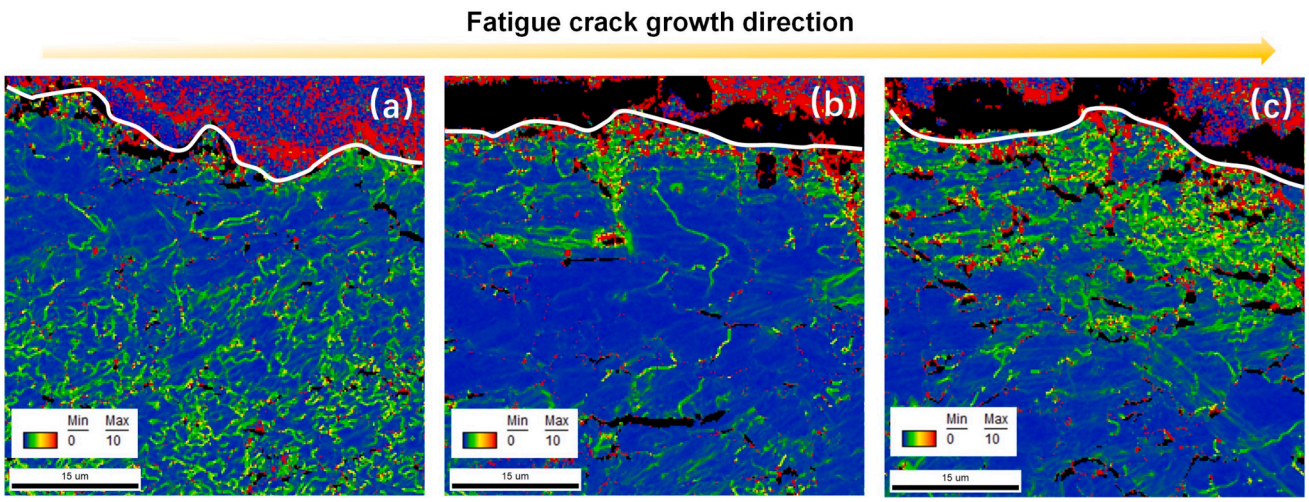

Fig. 16. The corresponding Kernel Average Misorientation (KAM) maps resulted from EBSD analyses for the E-WM material. (Global FCG direction is from left to right, the white lines indicate crack growth paths).

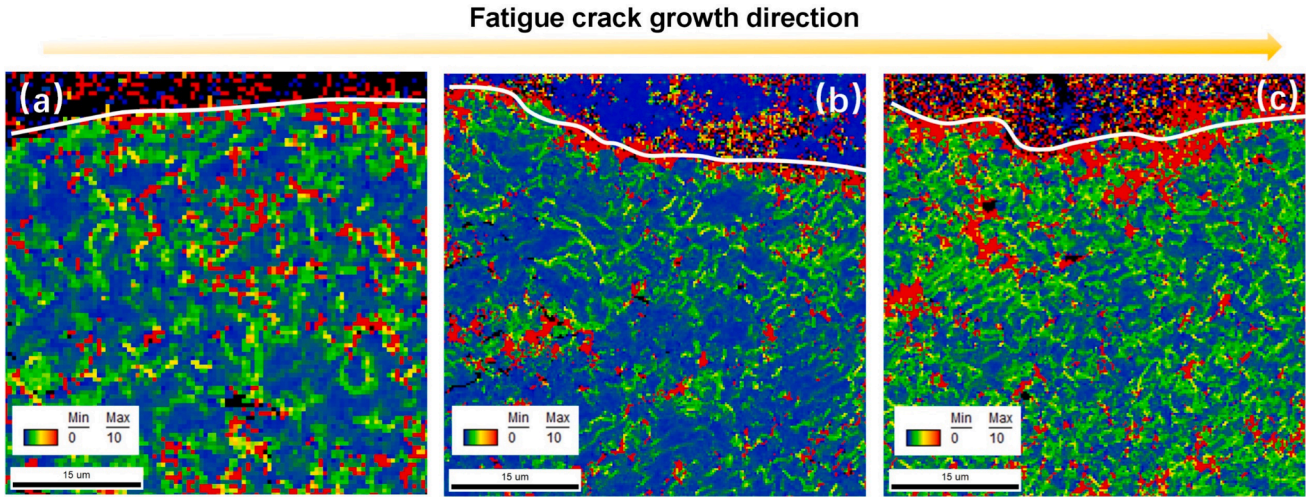

Fig. 17. The corresponding Kernel Average Misorientation (KAM) maps resulted from EBSD analyses for the U-WM material. (Global FCG direction is from left to right, the white lines indicate crack growth paths).

Fig. 18 and Fig. 19. According to the typical fractography of E-WM (Fig. 18), many parallel fatigue striations and edges nearly perpendicular to the crack propagation direction were observed in different growth regimes. The distance between striations in E-WM is gradually more extensive from the initial crack regime to the accelerated growth regime. Generally, the fatigue striations and existed edges are related to the level of ΔK. However, the fatigue striations were not exhibited obviously. Only in the accelerated growth regimes shows the fatigue striation marks slightly. The different characteristic appearance of striation morphology is dependent on the material microstructures. Moreover, several short secondary microcracks can be observed clearly beneath the fracture surface in different regimes. Compared with U-WM in Fig. 19, few tiny secondary microcracks perpendicular to the direction of crack growth exist in the accelerated growth regime in fracture surfaces of BM specimens.

The comparison between fracture morphologies of E-WM and U-WM in the final failure regime is shown by Fig. 19 (g) (h) and Fig. 19 (g) (h). Substantial dimples can be seen on the fracture surfaces for these two materials, which indicate a ductile fracture mechanism induced by micro-void coalescence. The dimples on the fracture surface of the E-WM specimen are deeper than the U-WM specimen, showing typical ductile fracture morphology for metallic materials. It further indicates E-WM has stronger plastic deformation ability than the U-WM. It should be noticed that plenty of secondary particles in the E-WM fracture surface were shown in Fig. 19(h). The ductile fracture surface of the final stage was scanned and analyzed by Energy Dispersive Spectrometry (EDS). The scanning spots and energy spectra are shown in Fig. 20. The EDS results indicate that the particles are mainly Ti-rich inclusions, which possibly came from the weld filler during the cooling stage of the welding process.

3.8. Discussion

To apply the fatigue properties for the fatigue reliability assessment of engineering structures, the relationship between the fatigue properties and welded joints geometries should be clarified. On the one hand, the fatigue crack growth properties for BM and weldments can be employed to predict the fatigue propagation life for different welded joints or complex welded components [22,49]. A low cycle fatigue based FCG model could be used to predict the long and physically short crack, and further expended to realize the fatigue life prediction of components for engineering applications [50]. Combined with the fatigue reliability theory, some deficiency of computational results with conventional fatigue assessment approaches would be examined considering various

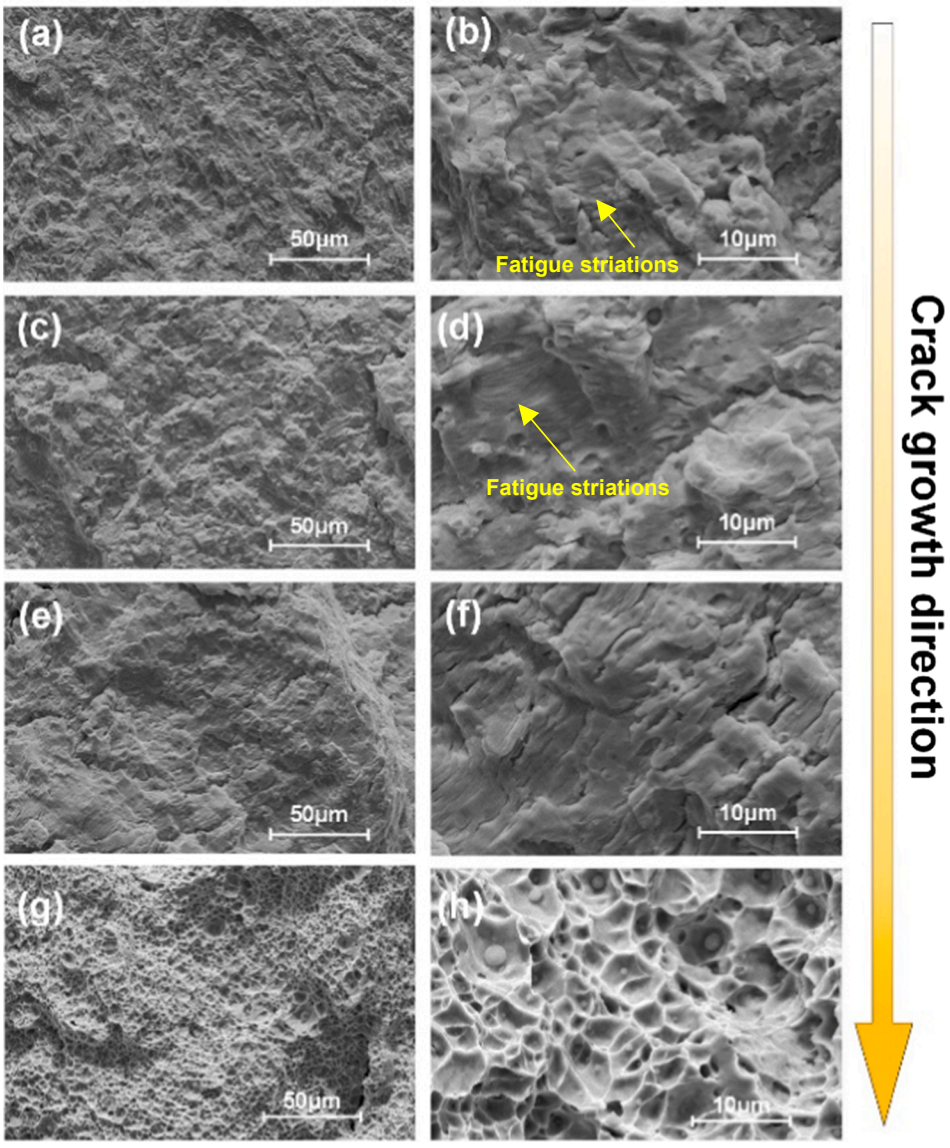

Fig. 18. Typical fractography of E-WM specimens under different regimes by different scales (10 μm and 50 μm). (a) and (b) initial crack growth regime, (c) and (d) intermediate growth regime, (e) and (f) accelerated growth regime, (g) and (h) ductile fracture zone.

effects on the basis of notch concept in HCF regimes, such as the weldment random geometrical details, residual stress effect [51], fatigue loading conditions, service conditions [52], crack propagation threshold and misalignment [53,54]. On the other hand, the fatigue properties of materials in LCF regime can be utilized to estimate the fatigue initiation life under different fatigue loading modes. Under the stress-controlled loading mode, the ratchetting-fatigue interaction could be illustrated by ductility exhaustion theory and continuum damage mechanics [55]. The cyclic soften or hardening behavior is also significant effect in LCF assessment of the welded joints [56]. Thus, the fatigue properties of materials in LCF regime are the substantial parameters to estimate the fatigue life of welded joints and components.

4. Conclusions

The present paper studies fatigue crack growth behavior of 10CrNi3MoV high strength steel evenmatched (E-WM) and undermatched (U-WM) weldments by different characteristic methods. The effects of microstructure, welding residual stress and stress ratio were analyzed and discussed. Based on the above studies, the following conclusions are drawn:

(1) For the low R-ratio ($R = 0.1$), the U-WM demonstrates higher FCGR curves than that in the BM and E-WM. The carbides in mixed pearlite and ferrite microstructure exhibits lower fatigue crack growth resistance than the mixed binate and ferrite microstructures of E-WM. Ti-rich inclusion in E-WM can be beneficial to stimulate the nucleation of acicular ferrite and further elevate the fatigue crack growth resistance. Besides, there is no significant difference of FCGR for E-WM and U-WM between high R-ratios (0.4 and 0.7).

(2) Two different fracture mechanisms are exhibited for E-WM and U-WM. Transgranular fracture appearances were shown on E-WM, while the intergranular fracture surfaces were observed on U-WM. Plenty of secondary particles in the E-WM fracture surface exist, while few tiny secondary microcracks perpendicular to the direction of crack growth are observed in the U-WM accelerated growth regime, indicating that the U-WM has better ductility than E-WM.

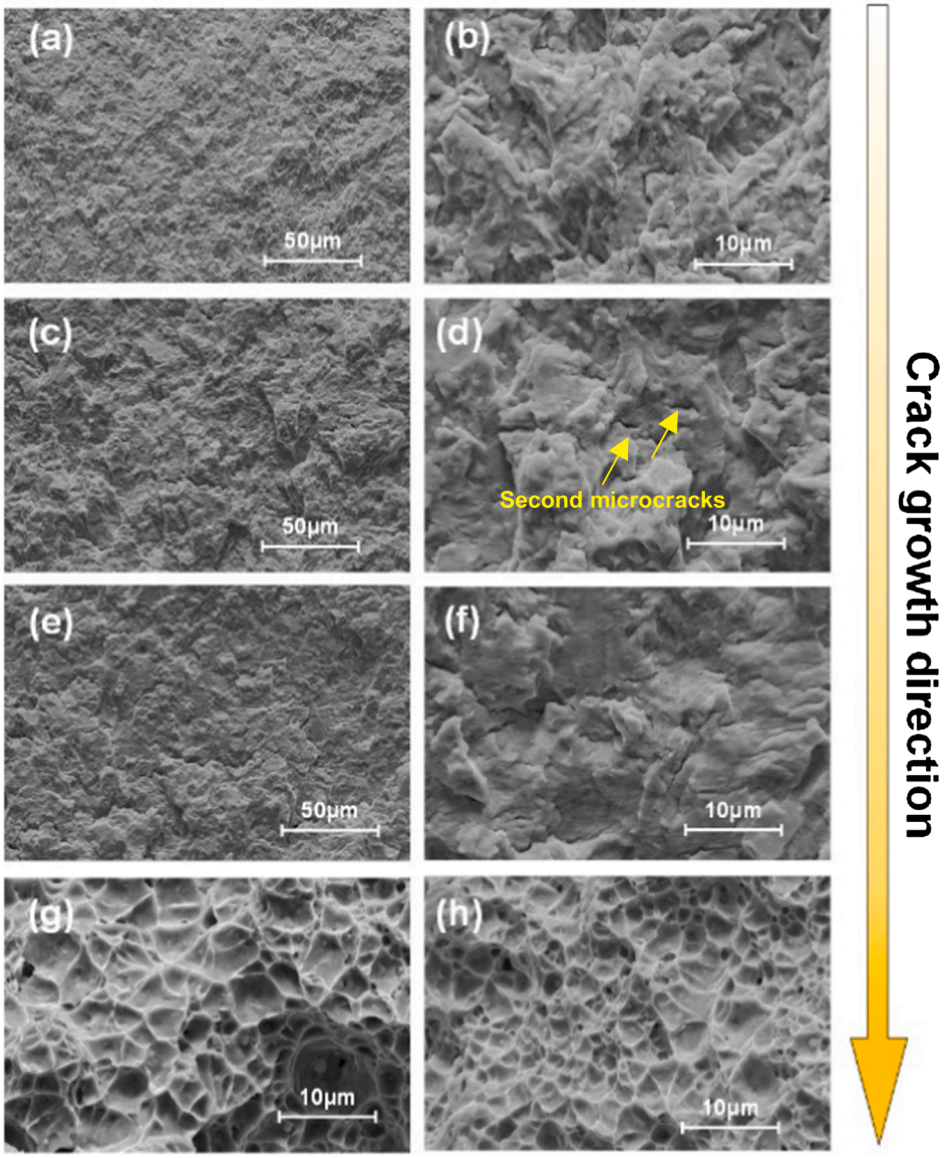

Fig. 19. Typical fractography of U-WM specimens under different regimes by different scales (10 μm and 50 μm). (a) and (b) initial crack growth regime, (c) and (d) intermediate growth regime, (e) and (f) accelerated growth regime, (g) and (h) ductile fracture zone.

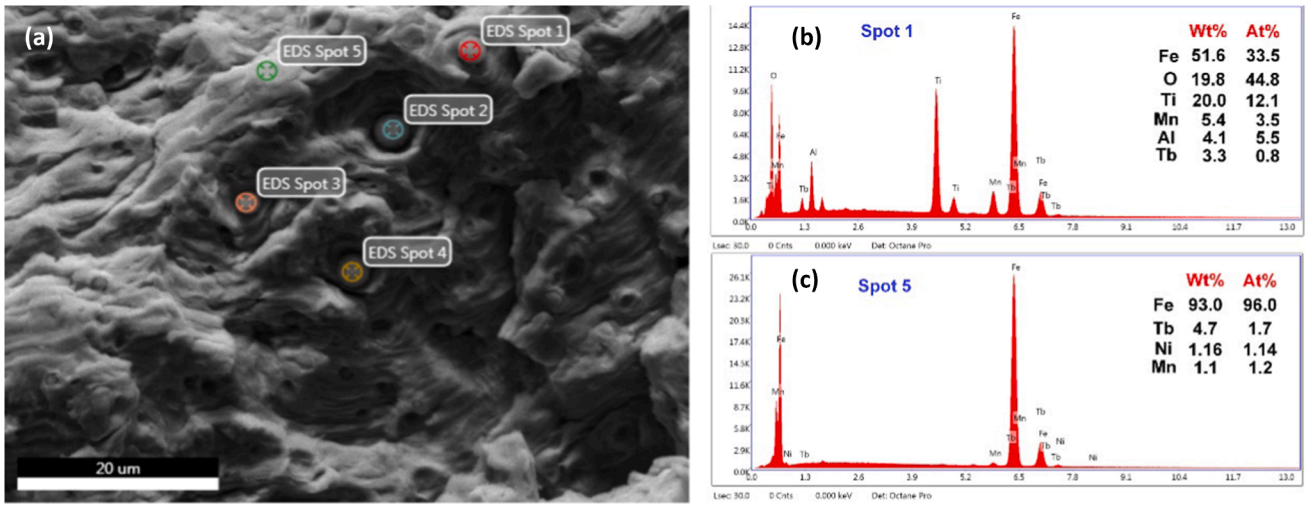

Fig. 20. (a) SEM image of a secondary particle on the fracture surface of the E-WM and (b) EDS profiles of the particle. (c) EDS profiles of base metal.

(3) The FCGR of base metal and weldments have been evaluated under as-welded and PWHT. The results demonstrate that residual stress in the extracted CT specimens has noticeably influenced the FCGR of E-WM and U-WM. Regarding the E-WM specimens, the FCGR in the as-welded state is less than in the PWHT state due to compressive residual stresses. As for U-WM specimens at $R = 0.1$ and 0.4, FCGR under the as-welded state is slightly lower than PWHT state, attributing to the tensile residual stress effect on fatigue crack tip.

(4) According to the KAM analysis, the plastic deformation in the crack extension accelerated regime is heavier than the initial and stable stages for both E-WM and U-WM by comparison with three different crack growth regimes. More advanced characterization methods may be applied to study the fundamental mechanism of the material heterogeneity cracking phenomena in the future.

Statements of contribution

Wei Song and Xuesong Liu together proposed this methodology. Wei Song did finite element analysis and calculations. Ping Wang helped to study and explain the experimental data. Di Wan helped to illustrate the microstructure mechanism of fatigue fracture in the paper. Filippo Berto supervised the findings of this work. Guian Qian and José Correia revised the manuscript. All authors discussed the results and contributed to the final manuscript.

Declaration of Competing Interest

The authors declare that they have no known competing financial interests or personal relationships that could have appeared to influence the work reported in this paper.

Acknowledgements

The research project is supported by the Natural Science Foundation of Jiangsu Province (grant no. BK20200174), he Natural Science Foundation of the Higher Education Institutions of Jiangsu Province (grant no. 20KJB430008), and the Qinglan Project in Jiangsu Province.

References

[1] Venezuela J, Zhou Q, Liu Q, Li H, Zhang M, Dargusch MS, et al. The influence of microstructure on the hydrogen embrittlement susceptibility of martensitic advanced high strength steels. Mater Today Commun 2018;17:1–14.
[2] Liu Q, Zhou Q, Venezuela J, Zhang M, Wang J, Atrens A. A review of the influence of hydrogen on the mechanical properties of DP, TRIP, and TWIP advanced high-strength steels for auto construction. Corros Rev 2016;34:127–52.
[3] Venezuela J, Liu Q, Zhang M, Zhou Q, Atrens A. A review of hydrogen embrittlement of martensitic advanced high-strength steels. Corros Rev 2016;34:153–86.
[4] Dwivedi SK, Vishwakarma M. Effect of hydrogen in advanced high strength steel materials. Int J Hydrogen Energy 2019;44:28007–30.
[5] Takagi S, Toji Y, Yoshino M, Hasegawa K. Hydrogen embrittlement resistance evaluation of ultra high strength steel sheets for automobiles. ISIJ Int 2012;52:316–22.
[6] Todoshchenko O, Yagodzinskyy Y, Yagodzinska V, Saukkonen T, Hänninen H. Hydrogen effects on fracture of high-strength steels with different micro-alloying. Corros Rev 2015;33:515–27.
[7] Younes CM, Steele AM, Nicholson JA, Barnett CJ. Influence of hydrogen content on the tensile properties and fracture of austenitic stainless steel welds. Int J Hydrogen Energy 2013;38(11):4864–76.
[8] Hoyos JJ, Masoumi M, Pereira VF, Tschiptschin AP, Paes MTP, Avila JA. Influence of hydrogen on the microstructure and fracture toughness of friction stir welded plates of API 5L X80 pipeline steel. Int J Hydrogen Energy 2019;44(41):23458–71.
[9] Viano DM, Ahmed NU, Schumann GO. Influence of heat input and travel speed on microstructure and mechanical properties of double tandem submerged arc high strength low alloy steel weldments. Sci Technol Weld Joining 2000;5(1):26–34.
[10] Barbosa Luiz Henrique Soares, Modenesi Paulo José, Godefroid Leonardo Barbosa, Arias Ariel Rodriguez. Fatigue crack growth rates on the weld metal of high heat input submerged arc welding. Int J Fatigue 2019;119:43–51.
[11] Liu X, Chung K-F, Ho H-C, Xiao M, Hou Z-X, Nethercot DA. Mechanical behavior of high strength S690-QT steel welded sections with various heat input energy. Eng Struct 2018;175:245–56.
[12] Zhai Y, Huang B, Zhang Z, Mao X, Zhao Z. Effect of preheating on welding cold crack sensitivity of China low activation martensitic steel. Fusion Eng Des 2018;133:32–8.
[13] Dai T, Lippold JC. The effect of postweld heat treatment on hydrogen-assisted cracking of 8630/Alloy 625 overlay. Weld World 2018;62:581–99.
[14] Zhao MC, Yang K, Shan Y. The effects of thermo-mechanical control process on microstructures and mechanical properties of a commercial pipeline steel. Mater Sci Eng, A 2002;335:14–20.
[15] Xiong Z, Liu Shi, Wang X, et al. The contribution of intragranular acicular ferrite microstructural constituent on impact toughness and impeding crack initiation and propagation in the heat-affected zone (HAZ) of low-carbon steels. Mater Sci Eng, A 2015;636:117–23.
[16] Zong L, Shi G, Wang Q. Experimental investigation on fatigue crack behavior of bridge steel Q345qD base metal and butt weld. Mater Des 2015;66:196–208.
[17] Wang Q, Yan Z, Liu X, Dong Z, Fang H. Understanding of fatigue crack growth behavior in welded joint of a new generation Ni-Cr-Mo-V high strength steel. Eng Fract Mech 2018;194:224–39.
[18] Zhu M-L, Xuan F-Z, Wang G-Z. Effect of microstructure on fatigue crack propagation behavior in a steam turbine rotor steel. Mater Sci Eng, A 2009;515:85–92.
[19] Liu Shi-Dong, Zhu Ming-Liang, Zhou Hai-Bo, Wan Di, Xuan Fu-Zhen. Strain visualization of growing short fatigue cracks in the heat-affected zone of a Ni–Cr–Mo–V steel welded joint: Intergranular cracking and crack closure. Int J Press Vessels Pip 2019;178:103992. https://doi.org/10.1016/j.ijpvp.2019.103992.
[20] Ronevich Joseph A, Song Eun Ju, Feng Zhili, Wang Yanli, D'Elia Christopher, Hill Michael R. Fatigue crack growth rates in high pressure hydrogen gas for multiple X100 pipeline welds accounting for crack location and residual stress. Eng Fract Mech 2020;228:106846. https://doi.org/10.1016/j.engfracmech.2019.106846.
[21] Li S, Kang Y, Zhu G, Kuang S. Microstructure and fatigue crack growth behavior in tungsten inert gas welded DP780 dual-phase steel. Mater Des 2015;85:180–9.
[22] Zong L, Shi G, Wang Y. Experimental investigation and numerical simulation on fatigue crack behavior of bridge steel WNQ570 base metal and butt weld. Constr Build Mater 2015;77:419–29.
[23] de Jesus AMP, Matos R, Fontoura BFC, Rebelo C, Simões da Silva L, Veljkovic M. A comparison of the fatigue behavior between S355 and S690 steel grades. J Constr Steel Res 2012;79:140–50.
[24] Lukács J, Dobosy Á. Matching effect on fatigue crack growth behaviour of high-strength steels GMA welded joints. Weld World 2019;63:1315–27.
[25] Zhang C, Lu P, Hu X, Song X. Residual stress-induced deformation and fatigue crack growth in weld-repaired high-strength low-alloy steel with soft buffer layer. Mater Sci Eng, A 2013;564:147–57.
[26] Mehmanparast A, Brennan F, Tavares I. Fatigue crack growth rates for offshore wind monopile weldments in air and seawater: SLIC inter-laboratory test results. Mater Des 2017;114:494–504.
[27] Yun W, Philip B, Zhenying X, Junfeng W. Study on fatigue crack growth performance of EH36 weldments by laser shock processing. Surf Interfaces 2019;15:199–204.
[28] Huang X, Moan T. Improved modeling of the effect of R-ratio on crack growth rate. Int J Fatigue 2007;29:591–602.
[29] Li Y, Wang H, Gong D. The interrelation of the parameters in the Paris equation of fatigue crack growth. Eng Fract Mech 2012;96:500–9.
[30] Sadananda K, Vasudevan AK. Fatigue crack growth mechanisms in steels. Int J Fatigue 2003;25:899–914.
[31] McClung RC. The influence of applied stress, crack length, and stress intensity factor on crack closure. Metall Trans A 1991;22:1559–71.
[32] Newman JC. A crack opening stress equation for fatigue crack growth. Int J Fract 1984;24(4):R131–5.
[33] McEvily AJ, Ritchie RO. Crack closure and the fatigue-crack propagation threshold as a function of load ratio. Fatigue Fract Eng Mater Struct 1998;21:847–55.
[34] Jacob A, Mehmanparast A, D'Urzo R, Kelleher J. Experimental and numerical investigation of residual stress effects on fatigue crack growth behaviour of S355 steel weldments. Int J Fatigue 2019;128:105196.
[35] Ravi Chandran KS, Galyon Dorman SE. The nature of specimen-size-effect on fatigue crack growth and net-section fracture mechanics approach to extract the size-independent behavior. Int J Fatigue 2021;145:106088.
[36] . Tabernig, P. Powell, R. Pippan, Fatigue Crack Growth Thresholds, Endurance Limits, and Design, (2000).
[37] Forth SC, Newman Jr JC, Formar RG. Anomalous fatigue crack growth data generated using the ASTM standards, in. ASTM Spec Tech Publ 2007:244–55.
[38] Song W, Liu X, Berto F, Razavi SMJ. Low-Cycle Fatigue Behavior of 10CrNi3MoV High Strength Steel and Its Undermatched Welds. Materials (Basel) 2018;11:661.
[39] B.S. Institution, Metallic materials - Fatigue testing - Fatigue crack growth method, in: BS ISO 12108:2012, London, 2012.
[40] Yuhang Lou HX, Peng Yun. Study on microstructure and properties of welded joints of a 690 MPa grade HSLA steel. Mater Sci Technol 2012;20:101–7.
[41] Shahani AR, Shakeri I. Experimental evaluation of fatigue behaviour of thin Al5456 welded joints. Fatigue Fract Eng Mater Struct 2020;43:965–77.
[42] A.F. Hobbacher, Recommendations for Fatigue Design of Welded Joints and Components, IIW Collection, in: Recommendations for Fatigue Design of Welded Joints and Components, London, 2016.
[43] Huang S, Zhou JZ, Sheng J, Luo KY, Lu JZ, Xu ZC, et al. Effects of laser peening with different coverage areas on fatigue crack growth properties of 6061–T6 aluminum alloy. Int J Fatigue 2013;47:292–9.

[44] Pavan M, Furfari D, Ahmad B, Gharghouri MA, Fitzpatrick ME. Fatigue crack growth in a laser shock peened residual stress field. Int J Fatigue 2019;123:157–67.
[45] Zhang Z, Ma H, Zheng R, Hu Q, Nakatani M, Ota M, et al. Fatigue behavior of a harmonic structure designed austenitic stainless steel under uniaxial stress loading. Mater Sci Eng, A 2017;707:287–94.
[46] Sachs NW. Understanding the surface features of fatigue fractures: how they describe the failure cause and the failure history. J Fail Anal Prev 2005;5:11–5.
[47] Schijve J. Fatigue as a phenomenon in the material. Springer; 2001.
[48] Suresh S. Fatigue of Materials 2004.
[49] Zong L, Shi G, Wang YQ, Li ZX, Ding Y. Experimental and numerical investigation on fatigue performance of non-load-carrying fillet welded joints. J Constr Steel Res 2017;130:193–201.
[50] Wu SC, Xu ZW, Yu C, Kafka OL, Liu WK. A physically short fatigue crack growth approach based on low cycle fatigue properties. Int J Fatigue 2017;103:185–95.
[51] Xin H, Correia JAFO, Veljkovic M, Berto F, Manuel L. Residual stress effects on fatigue life prediction using hardness measurements for butt-welded joints made of high strength steels. Int J Fatigue 2021;147:106175.
[52] Hu Y, Wu S, Withers PJ, Cao H, Chen P, Zhang Y, et al. Corrosion fatigue lifetime assessment of high-speed railway axle EA4T steel with artificial scratch. Eng Fract Mech 2021;245:107588.
[53] Dong Y, Garbatov Y, Guedes Soares C. Strain-based fatigue reliability assessment of welded joints in ship structures. Mar struct 2021;75:102878.
[54] Dong Y, Garbatov Y, Guedes Soares C. Improved effective notch strain approach for fatigue reliability assessment of load-carrying fillet welded cruciform joints in low and high cycle fatigue. Mar struct 2021;75:102849. https://doi.org/10.1016/j.marstruc.2020.102849.
[55] Luo H, Kang G, Kan Q. A low-cycle fatigue life-prediction model for SUS301L stainless steel butt-welded joint with considering ratchetting. Int J Fatigue 2020;139:105777.
[56] Song W, Liu X, Berto F, Razavi SMJ. Energy-based low cycle fatigue indicator prediction of non-load-carrying cruciform welded joints. Theor Appl Fract Mech 2018;96:247–61.